



저작자표시-비영리-변경금지 2.0 대한민국

이용자는 아래의 조건을 따르는 경우에 한하여 자유롭게

- 이 저작물을 복제, 배포, 전송, 전시, 공연 및 방송할 수 있습니다.

다음과 같은 조건을 따라야 합니다:



저작자표시. 귀하는 원저작자를 표시하여야 합니다.



비영리. 귀하는 이 저작물을 영리 목적으로 이용할 수 없습니다.



변경금지. 귀하는 이 저작물을 개작, 변형 또는 가공할 수 없습니다.

- 귀하는, 이 저작물의 재이용이나 배포의 경우, 이 저작물에 적용된 이용허락조건을 명확하게 나타내어야 합니다.
- 저작권자로부터 별도의 허가를 받으면 이러한 조건들은 적용되지 않습니다.

저작권법에 따른 이용자의 권리는 위의 내용에 의하여 영향을 받지 않습니다.

이것은 [이용허락규약\(Legal Code\)](#)을 이해하기 쉽게 요약한 것입니다.

[Disclaimer](#)

Master of Science

Effects of fluorine doping in lithium iron pyrophosphate by  
studies of XRD, MAS NMR and galvanostat

The Graduate School of the University of Ulsan

Department of Chemistry

Chaewon Moon

Effects of fluorine doping in lithium iron pyrophosphate by studies of  
XRD, MAS NMR and galvanostat

Supervisor Professor Youngil Lee

A Dissertation

Submitted to

The Graduate School of the University of Ulsan

In partial fulfillment of the requirements

for the degree of

Master of Science

by

Chaewon Moon

Department of Chemistry

University of Ulsan, Ulsan, Korea

January 2020

Effects of fluorine doping in lithium iron pyrophosphate by  
studies of XRD, MAS NMR and galvanostat

This certifies that the dissertation of Chaewon Moon is approved.

---

Committee Chair Dr. Jiwon ha

---

Committee Member Dr. Jaehoon Jung

---

Committee Member Dr. Youngli Lee

Department of Chemistry

Ulsan, Korea

January 2020

## Abstract

As a cathode material, lithium metal pyrophosphates,  $\text{Li}_2\text{MP}_2\text{O}_7$  ( $\text{M} = \text{Mn}, \text{Co}, \text{Fe}, \text{V}$ ), have been subjected to intense recent research. Pyrophosphate of the kind have a two-dimensional lithium diffusion channel along the crystallographic b and c axis and extracting more than one lithium ion per formula unit is possible. Among them,  $\text{Li}_2\text{FeP}_2\text{O}_7$  (LFPO) shows superior ionic diffusivity, inferior electronic conductivity and structural stability due to strong P–O bond as polyanion. Its theoretical reversible capacity is  $110 \text{ mAh g}^{-1}$  per  $1 \text{ e}^-$ . Anion doping into the polyanion site can be able to improve intrinsic electrochemical properties such as band gap and enhance lithium diffusion limitations. In this study, fluorine anion ( $\text{F}^-$ ) has been selected as a dopant in for oxygen sites. The fluorine doped LFPO has been synthesized by solid state reaction method. The structural study of the material has been investigated by X-ray diffraction and  $^7\text{Li}$  MAS NMR. And the electrochemical properties of samples have been carefully investigated through lithium extraction/inserting processes using galvanostatic charge/discharge and cyclic voltammetry (CV) measurements so as to investigate for Li ion transfer between the active electrode materials.

## Contents

Abstract.....	4
List of tables .....	8
List of figures .....	8
1. Introduction .....	13
1.1 Principle of lithium-ion batteries .....	16
1.2 Cathode materials.....	20
1.2.1 Layered .....	22
1.2.2 Spinel.....	23
1.2.3 Polyanion-type cathode.....	24
1.3 Iron and Phosphate-based cathode material .....	25
1.3.1 Lithium iron phosphate (LiFePO <sub>4</sub> ).....	25
1.3.1 Lithium iron pyrophosphate (Li <sub>2</sub> FeP <sub>2</sub> O <sub>7</sub> ).....	27
1.4 Effect of fluorine-substituted cathode material.....	32

2. Introduction of Nuclear Magnetic Resonance (NMR) .....	34
2.1 The principle of NMR.....	34
2.1.1 Boltzmann distribution.....	40
2.1.2 $T_1$ (Spin-lattice relaxation) and $T_2$ (Spin-spin relaxation) .....	42
2.2 Solid-state NMR.....	46
2.2.1 Interaction-type in Solid-state NMR.....	48
2.2.2 Magic Angle Spinning (MAS) technique.....	49
2.2.3 Spin echo pulse sequence (Hahn echo) .....	52
2.2.4 Structural analysis using NMR for cathode materials .....	56
3. Experimental.....	58
3.1 Synthesis.....	58
3.2 General characterization .....	60
3.3 Electrochemical test .....	62
3.4 Solid-state MAS NMR study of cathode materials .....	64

4. Results and Discussion.....	68
4.1 General characterization of cathode materials.....	68
4.1.1 Thermo gravimetric (TG) and Differential Scanning Calorimetry (DSC).....	68
4.1.2 X-ray Diffraction (XRD) for structural characterization .....	70
4.1.3 Scanning Electron Microscopy (FE-SEM) and Transmission electron Microscopy (TEM) analysis for particle size and morphology .....	76
4.1.4 X-ray photoelectron spectroscopy (XPS).....	80
4.2 Electrochemical study of synthesized cathode materials.....	83
4.2.1 Charge-discharge properties, Rate performance and long cycle abilities.....	83
4.2.3 Cyclic voltammetry (CV) .....	87
4.3 MAS NMR for structural characterization.....	91
4.3.1 <sup>7</sup> Li MAS NMR.....	91
4.3.2 <sup>31</sup> P MAS NMR.....	93
5. Conclusions.....	95

6. Reference .....	96
--------------------	----

### List of tables

**Table 2.1** Short Guide to Accessible Nuclei for Different Types of Energy Storage Materials<sup>51</sup>

**Table 4.1** Lattice parameters of  $\text{Li}_2\text{FeP}_2\text{O}_7-x\text{F}_{2x}$  ( $x = 0$  and  $0.10$ )

### List of figures

**Figure 1.1** Diagram comparing the rechargeable lithium ion battery technologies as a function of volumetric ( $\text{Wh L}^{-1}$ ) and specific energy densities ( $\text{Wh kg}^{-1}$ ).<sup>5</sup>

**Figure 1.2** Schematic diagram of the lithium intercalation-de-intercalation reaction mechanism in a rechargeable lithium-ion battery.<sup>7</sup>

**Figure 1.3** Relative energy diagram of electrode potentials and electrolyte energy gap in LIBs<sup>7</sup>

**Figure 1.4** Schematic illustrations of various crystallographic structures of (a)  $\text{LiMO}_2$ , (b)  $\text{LiMn}_2\text{O}_4$  and (c)  $\text{LiFePO}_4$ . The small green balls represent  $\text{Li}^+$ .<sup>10</sup>

**Figure 1.5** Illustration of path-dependence in an electrode undergoing a shrinking core.<sup>26</sup>

**Figure 1.6** (a) Unit-cell structure of  $\text{Li}_2\text{MP}_2\text{O}_7$  and (b) Views from ab (left) and ac(right) planes of supercell structure.<sup>31</sup>

**Figure 1.7** Close-up view of edge-sharing between an  $\text{FeO}_6$  octahedron (fully occupied Fe1 site) and  $\text{FeO}_5/\text{LiO}_5$  polyhedral (mixed-occupied Fe2/Li4 and Li5/Fe3 sites)<sup>30</sup>

**Figure 1.8** Crystallographic structure of  $\text{Li}_2\text{FeP}_2\text{O}_7$  viewed along the c-axis. The three different local environments around iron are specifically indicated.<sup>32</sup>

**Figure 1.9** General strategies for performance enhancement and their rationale: (a) reducing dimensions of active materials, (b) formation of composites, (c) doping and functionalization, (d) tuning particle morphology, (e) formation of coatings or shells around active materials, (f) modification of electrolyte.<sup>33</sup>

**Figure 2.1** Periodic table of nuclear spin for NMR.<sup>52</sup>

**Figure 2.2** (a) No magnetization is present for the randomly orientated nuclear spins of the sample. (b) Longitudinal magnetization along the z-axis builds up as soon as a magnetic field  $B_0$  is applied. A net magnetic moment results.<sup>51</sup>

**Figure 2.3** Illustration of Zeeman Splitting of Energy levels.<sup>50, 53</sup>

**Figure 2.4** Schematic of principle of operation of conventional NMR<sup>50, 54</sup>

**Figure 2.5** Spin-lattice relaxation ( $T_1$ ) processes<sup>56</sup>

**Figure 2.6** Transverse ( $T_2$  and  $T_2^*$ ) relaxation processes<sup>56</sup>

**Figure 2.7** Comparison between spectra of solution  $^{13}\text{C}$  NMR and solid state  $^{13}\text{C}$  NMR.<sup>57</sup>

**Figure 2.8** A schematic representation of a transient sedimentation NMR experiment.<sup>59</sup>

**Figure 2.9** Illustration of magic angle spinning (MAS). (a) A pair of nuclear spins I and S in the solid-state NMR sample tube rotate along the axis tilted magic angle ( $54.741^\circ$ ) with

respect to the external magnetic field. (b) Rotation of the I–S internuclear vector under MAS is expressed by angles  $\alpha$  (azimuth angle; rotation of I–S vector around the spinning axis) and  $\beta$  (polar angle; tilt angle between the I–S vector and spinning axis)<sup>60, 61</sup>

**Figure 2.10** Schematic illustration of 1D NMR pulse sequence. (p1 = pulse width or duration, plw1 = RF field strength, aq = acquisition time and d1 = delay time)

**Figure 2.11** Representation of spin echo sequence. The NMR signal is measured according to the initial excitation pulse attenuation.

**Figure 3.1** Solid-state synthetic procedures of  $\text{Li}_2\text{FeP}_2\text{O}_7\text{-xF}_{2\text{x}}$  as a cathode material.

**Figure 3.2** Illustration of a coin cell type assembly.

**Figure 3.3** Bruker Avance III 300MHz NMR.

**Figure 3.4** Sampling kit for solid-state NMR.

**Figure 3.5** solid-state NMR rotors of various sizes

**Figure 3.6** The spin-echo (Hahn echo) pulse sequence of  $^7\text{Li}$  MAS NMR

**Figure 3.7** The spin-echo (Hahn echo) pulse sequence of  $^{31}\text{P}$  MAS NMR

**Figure 4.1** TG/DSC curve of the precursor under flowing nitrogen.

**Figure 4.2** The XRD pattern of  $\text{Li}_2\text{FeP}_2\text{O}_7$  sintered at each temperature. (a) 500, (b) 600, and (c) 650 .

**Figure 4.3** XRD patterns of  $\text{Li}_2\text{FeP}_2\text{O}_7\text{-xF}_{2\text{x}}$  for  $x =$  (a) 0, (b) 0.01, (c) 0.03, (d) 0.05, (e) 0.10, (f) 0.50 and (g) 1.00. Black lines represent lithium iron pyrophosphate reference and Blue lines are represented lithium iron phosphate.

**Figure 4.4** Rietveld refinements of the XRD patterns of  $\text{Li}_2\text{FeP}_2\text{O}_{7-x}\text{F}_{2x}$   $x =$  (a) 0 and (b) 1.00.

**Figure 4.5** SEM images of the  $\text{Li}_2\text{FeP}_2\text{O}_{7-x}\text{F}_{2x}$   $x =$  (a) 0, (b) 0.01, (c) 0.03, (d) 0.05, (e) 0.10, (f) 0.50 and (g) 1.00.

**Figure 4.6** EDX elemental mapping of the  $\text{Li}_2\text{FeP}_2\text{O}_{7-x}\text{F}_{2x}$   $x =$  (a) 0, (b) 0.01, (c) 0.03, (d) 0.05, (e) 0.10, (f) 0.50, and (g) 1.00.

**Figure 4.7** TEM images of (a)  $\text{Li}_2\text{FeP}_2\text{O}_7$ , (b)  $\text{Li}_2\text{FeP}_2\text{O}_{7-x}\text{F}_{2x}$  and HR-TEM image of (c)  $\text{Li}_2\text{FeP}_2\text{O}_7$ , (d)  $\text{Li}_2\text{FeP}_2\text{O}_{7-x}\text{F}_{2x}$ .

**Figure 4.8** XPS spectra of  $\text{Li}_2\text{FeP}_2\text{O}_7$  (a) survey, (b) Fe(2p), and spectra of  $\text{Li}_2\text{FeP}_2\text{O}_{6.9}\text{F}_{0.2}$  (c) Fe(2p), (d) F(1s).

**Figure 4.9** 1st charge-discharge profile of  $\text{Li}_2\text{FeP}_2\text{O}_{7-x}\text{F}_{2x}$  series  $x =$  (a) 0, (b) 0.01, (c) 0.03, and (d) 0.05.

**Figure 4.10** The rate performance at various C-rate of  $\text{Li}_2\text{FeP}_2\text{O}_{7-x}\text{F}_{2x}$  series  $x =$  (a) 0, (b) 0.01, (c) 0.03, and (d) 0.05.

**Figure 4.11** The long cycle ability at 1C of  $\text{Li}_2\text{FeP}_2\text{O}_{7-x}\text{F}_{2x}$  series  $x =$  (a) 0, (b) 0.01, (c) 0.03, and (d) 0.05.

**Figure 4.12** Voltammogram of  $\text{Li}_2\text{FeP}_2\text{O}_7$  synthesized at 650

**Figure 4.13** Cyclic voltammetry (CV) of  $\text{Li}_2\text{FeP}_2\text{O}_{7-x}\text{F}_{2x}$   $x =$  (a) 0, (b) 0.01, (c) 0.03, and (d) 0.05.

**Figure 4.14**  $^7\text{Li}$  MAS NMR spectra of the  $\text{Li}_2\text{FeP}_2\text{O}_{7-x}\text{F}_{2x}$  series  $x =$  (a) 0, (b) 0.01, (c) 0.03, (d) 0.05, and (e) 0.10 at 30 kHz. Isotropic peak is marked as dash line and the spinning

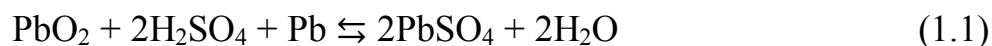
sidebands are marked with asterisks (\*).

**Figure 4.15**  $^{31}\text{P}$  MAS NMR spectra of the  $\text{Li}_2\text{FeP}_2\text{O}_7\text{-}_x\text{F}_{2x}$  series  $x =$  (a) 0, (b) 0.01, (c) 0.03, (d) 0.05, and (e) 0.10 at 30 kHz. Isotropic peak is marked as dash line and the spinning sidebands are marked with asterisks (\*).

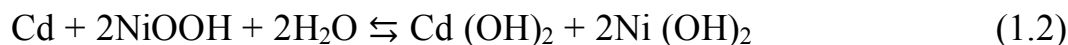
## 1. Introduction

Efforts to reduce dependence on fossil fuels require new forms of energy source and storage. Rechargeable batteries, also called secondary batteries differentiate from primary batteries by the feature of electrochemical reaction reversibility.<sup>1</sup> Compared to primary cells (not reversible), secondary batteries are more rentable, and core of future new growth power industry because it can charge and discharge numerous times. These energy storage devices can repeatedly go through 500 charge and discharge cycles, and reversibly convert electrical energy into chemical energy. The most common rechargeable batteries are lead-acid, Ni-Cd, Ni-MH and Li-ion. Small secondary batteries have found their applications in various portable devices including mobile phones, notebook computers, cameras, camcorders, personal digital assistants, medical instruments, and power tools.

In 1880s, the lead-acid battery has been commercialized. The electrochemical reaction of this battery is shown in Equation (1.1), and its open-circuit voltage (OCV) is about 2.0 V.



In 1901, Edison discovered the secondary nickel-cadmium (Ni-Cd) battery, which redox reaction is shown in Equation (1.2), and its OCV is about 1.35 V.



However, Ni-Cd batteries need periodic maintenance, and the usage of cadmium raised environmental issues due to the high cost of nickel and high self-discharge rate.<sup>2, 3</sup> To overcome the issue of low energy density of batteries, lithium-ion batteries have received great attention due to the largest weight capacity and the lowest redox potential. (Figure 1.1).

Lithium-ion batteries (LIBs) industry is undergoing rapid expansion, predicted to reach a market volume of tens of billions of dollars by the year 2020. represent a viable solution for hybrid and electrical vehicles (EVs), due to their high theoretical volumetric and gravimetric energy densities among known technologies.

LIBs usually consist of four main components: cathode, anode, electrolyte, and separator. Every single component of a LIB is essential as it can't function when one of the components is missing. The performance of the LIB is highly dependent on the cathode material. The first commercial LIBs was  $\text{LiCoO}_2$  that Sony corporation announced in the early 1990s.<sup>4</sup> Since then, various oxidized and poly-anion cathode compounds have been discovered.

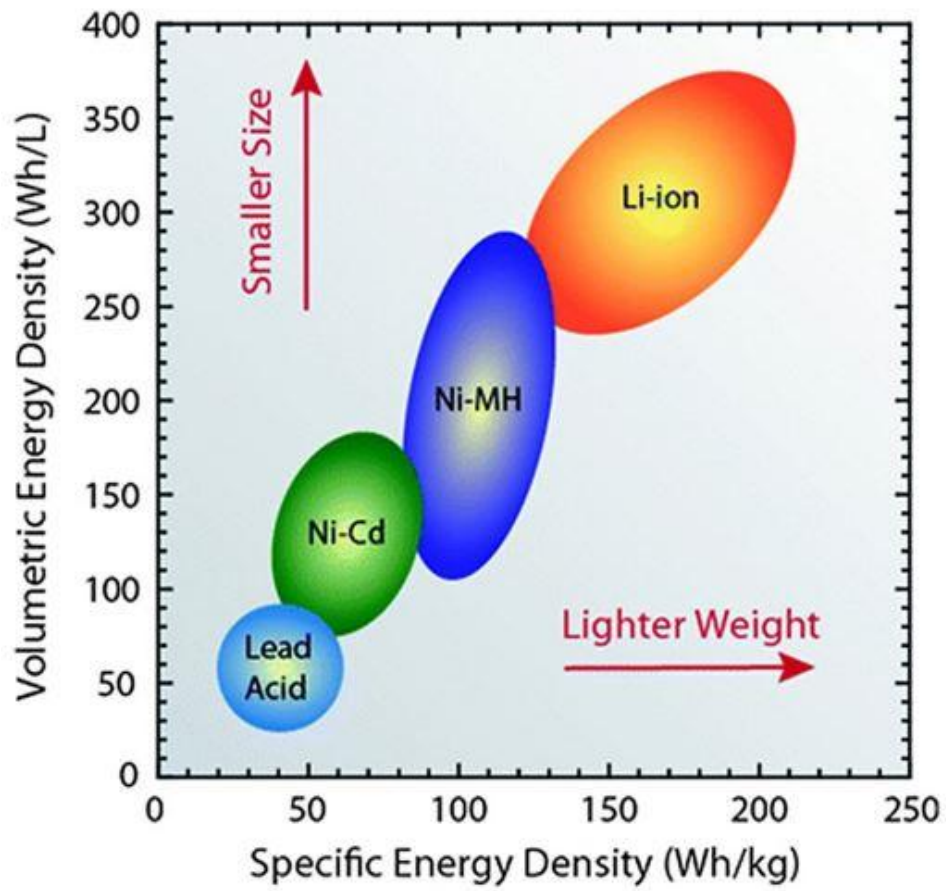
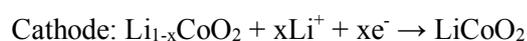


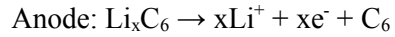
**Figure 1.1** Diagram comparing the rechargeable lithium-ion battery technologies as a function of volumetric ( $\text{Wh L}^{-1}$ ) and specific energy densities ( $\text{Wh kg}^{-1}$ ).<sup>5</sup>

## 1.1 Principle of lithium-ion batteries

Alternative energy technologies are actively being developed to reduce the use of fossil fuels. One of the approaches is the development of electrochemical energy that is sustainable and more environmentally friendly. The lithium-ion battery (LIB) is a representative system for such electrochemical energy storage and conversion. LIBs are one of the most promising energy storage technologies currently available and widely used in portable electronics. The worldwide market for rechargeable lithium-ion batteries are now valued at 10 billion dollars per annum and continuously growing. Recent demands for energy and environmental sustainability are undergoing rapid expansion, representing the largest portion of portable devices, efficient lightweight and rechargeable power supplies for consumer electronics such as laptop computers, digital cameras, and cell phones.

The lithium-ion battery is consists of four major components such as anode, cathode, electrolyte, and separator. An anode is the lithium-ion source of the lithium battery while cathode is the lithium-ion sink. The electrolyte, commonly organic solvents (e.g.,  $\text{LiPF}_6$ , which has been widely adopted in the manufacture of commercial lithium-ion batteries), provides paths for the migration of Li ions as well as the separation of ionic transport and electronic transport. <sup>6</sup> The energy storage mechanism of a lithium-ion battery is very simple. As shown in Figure 1.2, lithium-ion batteries generally consist of graphite negative electrodes (anode), non-aqueous electrolytes, and layered  $\text{LiCoO}_2$  positive electrode (cathode).<sup>7</sup> During charging process, the Li-ion deintercalates from the lithium metal oxide (e.g.  $\text{LiCoO}_2$ ) and passes through the Li-ion conductive electrolyte and intercalates to the layered graphite. Lithium-ion and electron generation occurs through the following reactions:





Full Cell Reaction:



The capacity (Q) and voltage (E) of a battery are theoretically determined by the electrode reactions according to the Faraday equation and Gibbs free energy change. The equation 1.3 and 1.4 are given by

$$(\Delta G): Q = nF/M \quad (1.3)$$

$$\Delta G = nFE \quad (1.4)$$

Where n is the number of electrons involved in stoichiometric reaction, F is the Faraday constant, and M is the equivalent molecular weight.<sup>8</sup> Lithium-ion batteries store electrical energy in electrodes made of lithium-intercalating compounds and perform oxidation and reduction processes occurring at both electrodes at the same time.

The selection of electrodes depends on their electrochemical potential value as well as their location on the HOMO-LUMO energy gap of the electrolyte. In the expression of the electrochemical potential,  $\mu_A$  is referred to as an anode and  $\mu_C$  is referred to as a cathode. For stable cells,  $\mu_A$  should be lower than the LUMO of the electrolyte, otherwise the electrolyte will be reduced, while  $\mu_C$  should be higher than the HOMO of the electrolyte to inhibit oxidation of the electrolyte as shown in Figure 1.3.<sup>9</sup>

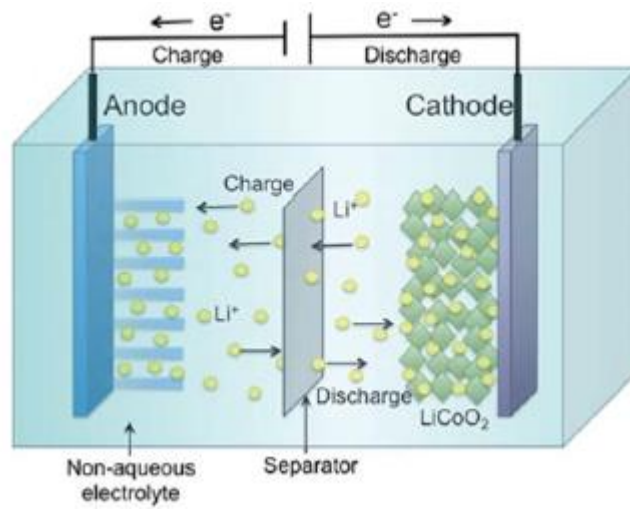


**Figure 1.2** Schematic diagram of the lithium intercalation-de-intercalation reaction mechanism in a rechargeable lithium-ion battery.<sup>7</sup>

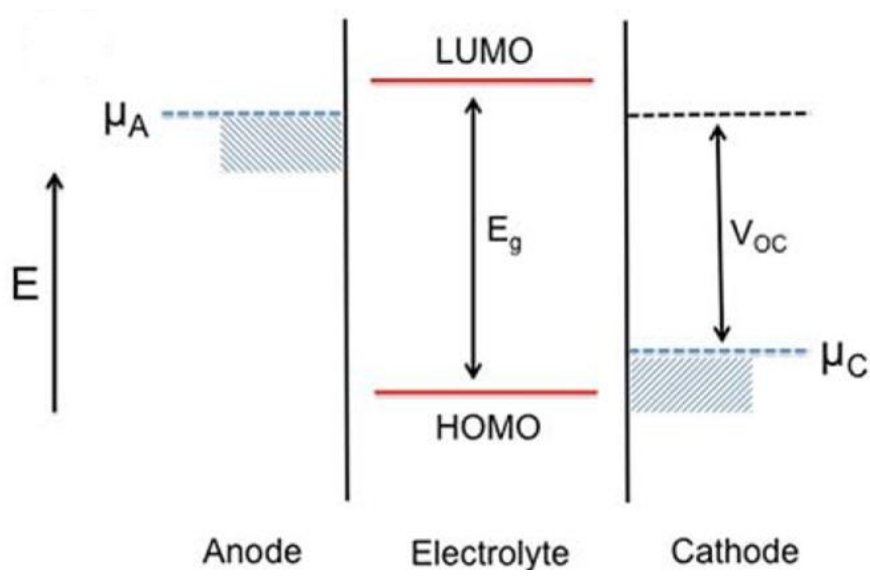


**Figure 1.3**

Relative energy diagram of electrode potentials and electrolyte energy gap in LIBs<sup>7</sup>

## 1.2 Cathode materials

The cathode material in Li-ion battery chemistry is the major and active source of all the Li-ions. It plays an important role in the determination of energy density, safety and life cycle of Li-ion batteries (LIBs). So, the electrochemical performance of LIBs is highly dependent on the structural characteristics of cathode material. Therefore, research and development of cathode materials is one of the popular topics on Li-ion batteries. Up to now, three main structural classes of cathode materials have been investigated, *i.e.* layered lithiated transition metal oxide, Mn-based spinel, and polyanion-type cathode materials. The schematic framework illustrations of the crystallographic structures for battery intercalation materials are depicted in Figure 1.4.<sup>10</sup>

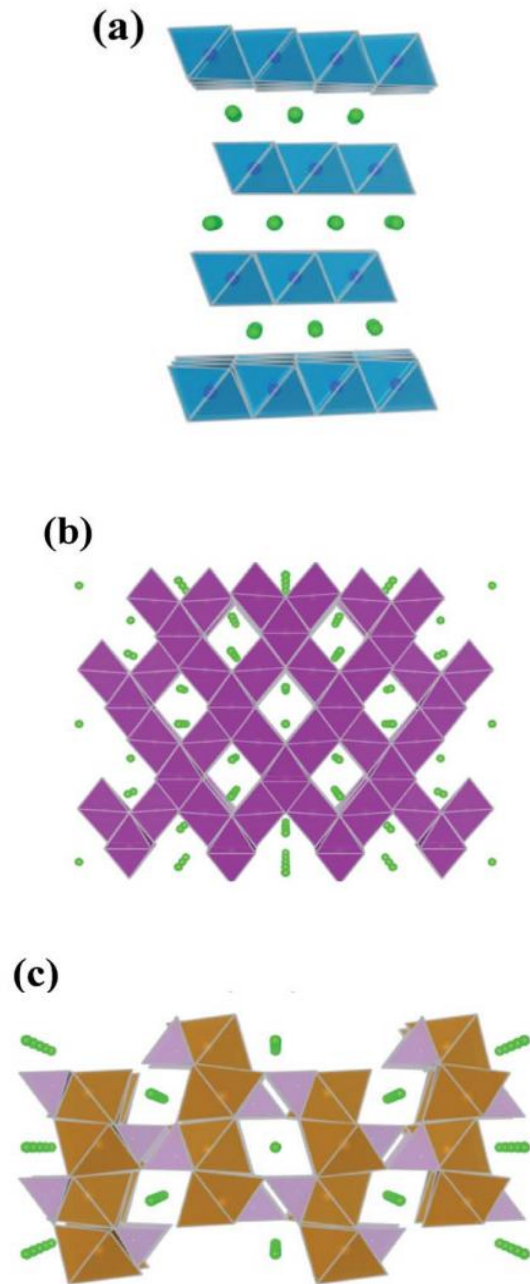


**Figure 1.4** Schematic illustrations of various crystallographic structures of (a)  $\text{LiMO}_2$ , (b)  $\text{LiMn}_2\text{O}_4$  and (c)  $\text{LiFePO}_4$ . The small green balls represent  $\text{Li}^+$ .<sup>10</sup>

### 1.2.1 Layered

Layered transition metal oxide cathode materials have several advantages: fully developed synthetic routes, high capacity and the ability for facile processing. A typical layered transition metal oxide cathode material is  $\text{LiCoO}_2$  (LCO). That was first commercialized LIB cathode material developed by Sony corporation in the early 1990s.<sup>11</sup> A stable structure of  $\text{LiCoO}_2$  is composed from alternating layers along the (1 1 1) planes in a cubic close-packed (CCP) oxygen array, in which Co and Li are located at distinct octahedral sites, to form a structure with overall hexagonal structure (space group R-3m).<sup>12</sup> Its practical capacity can reach  $140 \text{ mAh g}^{-1}$ , half of the theoretical capacity of  $274 \text{ mAh g}^{-1}$ , high theoretical volumetric capacity of  $1363 \text{ mAh cm}^{-3}$ , with a plateau potential of 3.9 V. Although  $\text{LiCoO}_2$  has excellent properties of charge-discharge profile and high specific capacity, cobalt has more toxic and expensive when it is compared to other transition metals. Moreover, compared to other potential electrode materials  $\text{LiCoO}_2$  is not stable and undergoes performance degradation during overcharging.<sup>13</sup> The degradation during cycling is caused by the dissolution of cobalt in the electrolyte when the electrode is desorbed during charging, thus a lower amount of lithium ions can be inserted in less amount during discharge. In addition, the  $\text{CoO}_2$  layer is formed after completely desorbing from the electrode surface.<sup>14</sup> Thus layered lithiated transition metal oxide like to LCO only used as electrode materials in small-scale batteries for portable electronic equipment.

## 1.2.2 Spinel

Mn-based spinel such as  $\text{LiMn}_2\text{O}_4$  has received a great deal of attention because it has abundant and low-cost starting materials. In general, spinel structure represented by  $\text{LiMn}_2\text{O}_4$  has 3D interstitial pathway for Li ion diffusion, as shown in Figure 1.4(b). It is important to note that the octahedral  $\text{MnO}_6$  shares the corners and forms a continuous 3D cubic array to provide the  $\text{Mn}_2\text{O}_4$  spinel structure robustness and stability. Due to the isotropic multi-directional Li ion diffusion, spinel structures with cubic symmetry can reach the highest Li ion conductivity among the intercalation materials. However, although spinel-type cathodes deliver a high discharge plateau, superior cycling, and outstanding rate capability, a capacity of barely less than  $150 \text{ mAh g}^{-1}$  is achieved during cycling at above 3 V. It can cause phase shift from cubic to tetragonal during the cycling by Jahn-Teller distortion. And, the capacity has been due to loss of oxygen during charging and dissolution of manganese through disproportionation in the electrolyte.<sup>15</sup>

### 1.2.3 Polyanion-type cathode

Polyanionic compounds generally consist of tetrahedral anions  $(\text{XO}_4)^{n-}$  and their derivatives  $(\text{X}_m\text{O}_{3m+1})^{n-}$  ( $\text{X} = \text{P}, \text{S}, \text{As}, \text{Mo}$  or  $\text{W}$ ) with strong covalent bonding combine with  $\text{MO}_x$  ( $\text{M} =$  transition metal) polyhedrons<sup>16</sup> These polyanions occupy lattice positions and increase cathode redox potential simultaneously stabilizing its structure. Thus, Polyanion cathode materials not only ensure the rapid conduction of alkali ions in the framework structure but also improve the structural stability during the metal redox process. The specific characteristics such as cycle stability, safety, environmental friendliness and potential low cost can make the most competent electrode material in future Li-ion batteries application like plug-in hybrid electric vehicles or ESS system. Since the first publication in 1997  $\text{LiMPO}_4$  ( $\text{M} = \text{Co}, \text{Fe}, \text{Mn}$ ) has attracted great interest because of their high voltages as well as their improved cycle life, high rates, low cost, and non-toxic nature.<sup>17</sup> Moreover, the  $\text{LiMPO}_4$  cathode materials are safer than the oxides due to their stability and provide good specific capacities. Among the polyanion compounds,  $\text{LiFePO}_4$  (see Figure 1.4(c)), which was firstly reported by J. Goodenough and have been widely investigated in the last two decades. The review of the recent status of polyanion compound cathode materials is imperative for future research in this field. However, further nanosizing entails volumetric capacities, restricting their applications where volume is not an issue. To overcome these limitations, variety polyanions have been investigated. Especially, Polyanions that can cycle multiple Li per unit cell have been a keen area of investigation with the pyrophosphates ( $\text{Li}_2\text{MP}_2\text{O}_7$ ) being proposed as promising candidates.<sup>18</sup>

## 1.3 Iron and Phosphate-based cathode material

### 1.3.1 Lithium iron phosphate (LiFePO<sub>4</sub>)

LiFePO<sub>4</sub> is the most widely studied and fully developed material among olivine phosphate and is generally considered to be one of the most promising battery materials used in Plug-in Hybrid Electric Vehicle/Electric Vehicle (PHEV/EV).

The olivine-type structure of LiFePO<sub>4</sub> can be described as a slightly distorted hexagonal close-packed (hcp) oxygen array resulting in an orthorhombic structure ( $D_{2h}$  – space group  $Pmnb$ ). Within the hcp oxygen framework, Li and M metal atoms are located in half of the octahedral sites and P atoms are located in 1/8 of the tetrahedral sites. The MO<sub>6</sub> octahedral share corners forming zigzag chains running parallel to the c-axis in the alternate a-c planes.

Its electrochemical properties were reported 20 years ago by Pahdi et al.<sup>19</sup> It remains the most commercially viable polyanion cathode due to the high safety and stability, low cost, high voltage (3.4 V vs Li<sup>0</sup>/Li<sup>+</sup>), and high theoretical capacity (170 mAh g<sup>-1</sup>).<sup>20</sup> However, the bulk LiFePO<sub>4</sub> does not exhibit sufficient rate performance because of their low conductivity ( $10^{-9} - 10^{-10}$  S cm<sup>-1</sup>) and do not well transfer Li-ions.<sup>21, 22</sup> To improve the electrochemical properties of LiFePO<sub>4</sub>, various methods, such as carbon coating<sup>23, 24</sup>, nanosizing<sup>25</sup> and ion substitution<sup>26</sup>, have been attempted to increase its electronic and ionic conductivities. The electrochemical reaction of LiFePO<sub>4</sub> is described in equation 1.5.



LiFePO<sub>4</sub> has charge and discharge process via a two-phase reaction between LiFePO<sub>4</sub> and FePO<sub>4</sub>. The process shown in Figure 1.5.

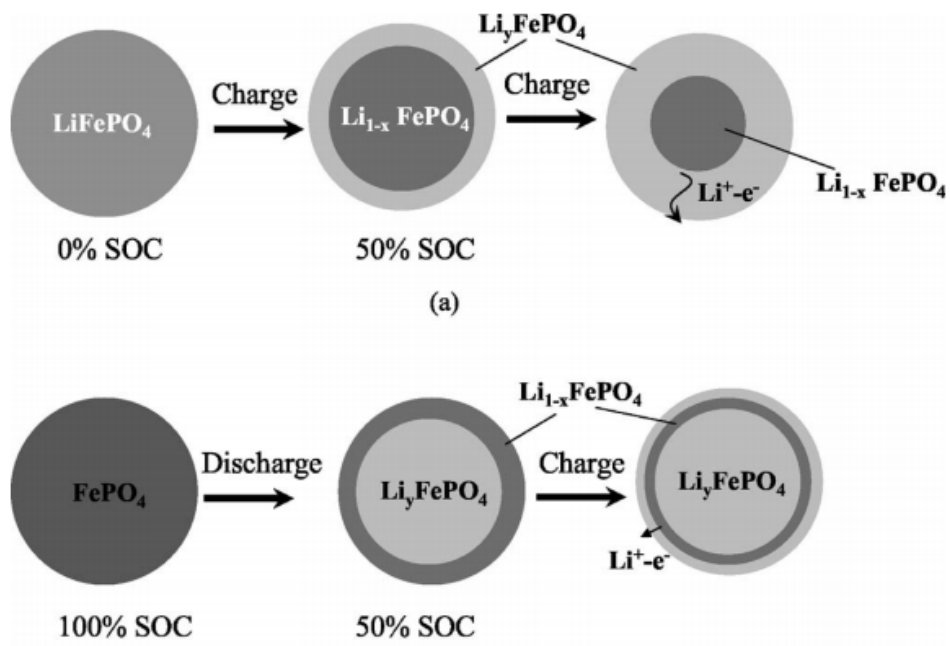


**Figure 1.5** Illustration of path-dependence in an electrode undergoing a shrinking core.<sup>27</sup>

### 1.3.1 Lithium iron pyrophosphate ( $\text{Li}_2\text{FeP}_2\text{O}_7$ )

An example of a new field of polyanionic cathode systems is the alkali metal pyrophosphate.  $\text{LiMP}_2\text{O}_7$  ( $M = \text{Fe}, \text{V}$ ) cathode were proposed in early 2000s as alternative electrode material which was based on a gamut of pyrophosphate ( $\text{P}_2\text{O}_7$ )<sup>4-</sup> compounds. Although all of these phosphates cathode materials are low-cost, high-voltage, and rare-metal free, their theoretical capacity is exceptionally small due to high molecular weight of pyrophosphate and low redox voltages.<sup>28-30</sup>

Compared to  $\text{LiFePO}_4$ , this pyrophosphate could realize one electron theoretical capacity without further carbon coating or particle downsizing. The alkali metal pyrophosphate compounds generally consist of transition metal with octahedral geometry ( $\text{MO}_6$ ) and  $\text{P}_2\text{O}_7$  units connected to form a robust three-dimensional framework. Also,  $\text{P}_2\text{O}_7$  units that chemical stability, possible multidimensional ionic conduction pathways and rich structural variation can hold potential for discovery of next generation electrodes.<sup>31</sup> Figure 1.6 shows the unit cell structure of  $\text{Li}_2\text{MP}_2\text{O}_7$ . Spheres represent  $\text{Li}^+$  ions, and polyhedrons are transition metals (deep blue and cyan) and phosphorus (pink) atoms. Crystallographically different sites are differentiated by their colors.<sup>32</sup>

Lithium iron pyrophosphate ( $\text{Li}_2\text{FeP}_2\text{O}_7$ ) have a two-dimensional (2D) lithium diffusion pathway and three-dimensional (3D) framework structure. The structure of  $\text{Li}_2\text{FeP}_2\text{O}_7$  reveals that the Fe1 sites ( $\text{FeO}_6$ ) are octahedrally coordinated while the Fe2 and Fe3 sites are coordinated as distorted  $\text{FeO}_5$  trigonal bipyramids. The P atoms are coordinated as corner sharing  $\text{PO}_4$  tetrahedron forming the ( $\text{P}_2\text{O}_7$ )<sup>4-</sup> diphosphate polyhedron units. The Fe polyhedrons are edge sharing and the three-edge sharing Fe polyhedron share a corner with one of the  $\text{PO}_4$  tetrahedrons of the ( $\text{P}_2\text{O}_7$ )<sup>4-</sup> diphosphate polyhedron units. The Fe2 and Fe3

atoms share their sites with lithium atoms Li5 and Li4, respectively. (Figure 1.7) The Li1 and Li3 atoms exist as edge sharing distorted LiO<sub>5</sub> trigonal bipyramids, while Li2 exists as a LiO<sub>4</sub> tetrahedron. The Li1, Li2 and Li3 atoms are stacked along the b–c plane, which may provide the possible pathways for lithium ion diffusion as shown in Figure 1.8.<sup>31, 33</sup>

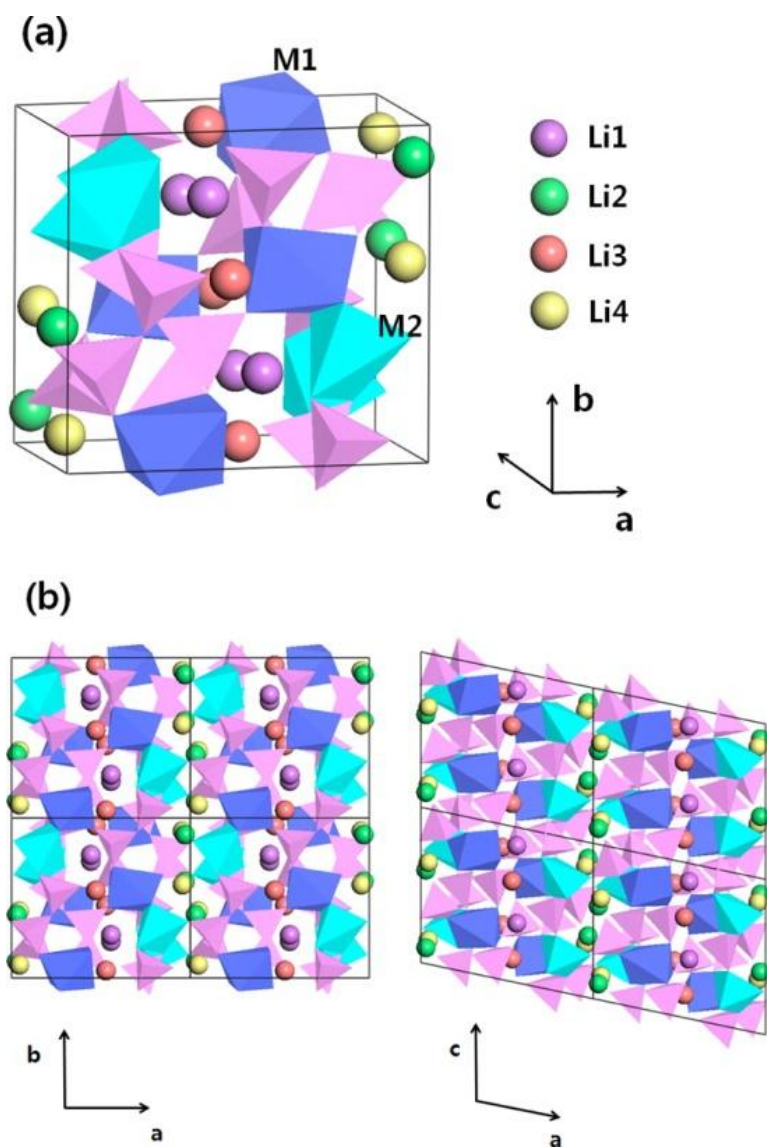


**Figure 1.6** (a) Unit-cell structure of  $\text{Li}_2\text{MP}_2\text{O}_7$  and (b) Views from ab( left) and ac( right) planes of supercell structure.<sup>32</sup>

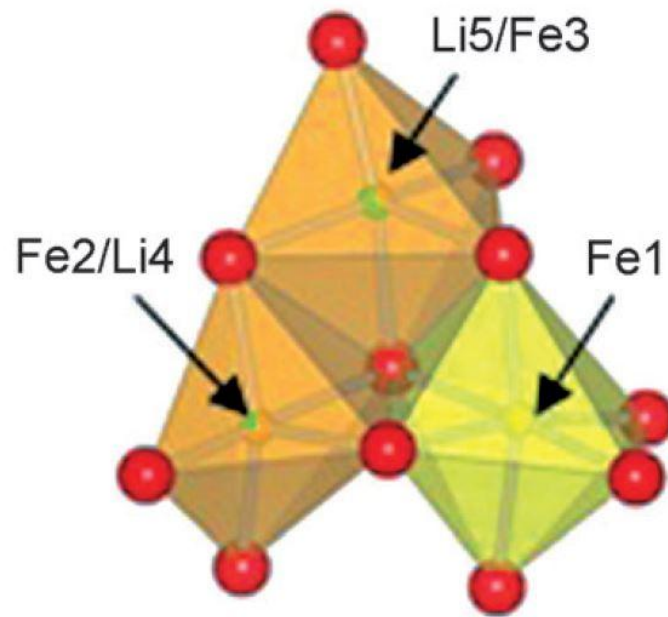


**Figure 1.7** Close-up view of edge-sharing between an  $\text{FeO}_6$  octahedron (fully occupied Fe1 site) and  $\text{FeO}_5/\text{LiO}_5$  polyhedra (mixed-occupied Fe2/Li4 and Li5/Fe3 sites).<sup>31</sup>

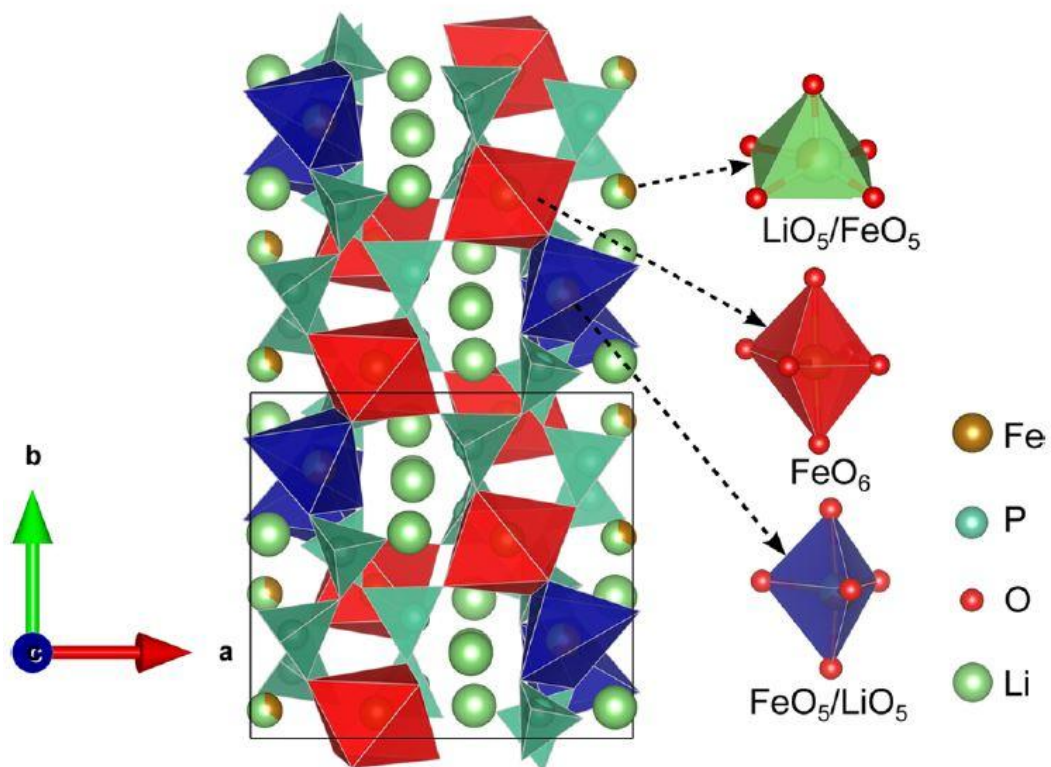


**Figure 1.8** Crystallographic structure of  $\text{Li}_2\text{FeP}_2\text{O}_7$  viewed along the  $c$ -axis. The three different local environments around iron are specifically indicated.<sup>33</sup>

## 1.4 Effect of fluorine-substituted cathode material

To enable the application of new types of electrode materials, there are various strategies such as dimension reduction, composite formation, doping, morphology control, etc. These strategies are summarized in Figure 1.9 and are often similar regardless of the type of material, crystal structure, or operating mechanism.<sup>34</sup>

Anion ( $F^-$ ,  $Cl^-$ , and  $S^{2-}$ ) or poly-anion substitution creates a high-rate positive electrode material due to increasing electrical conductivity at oxygen site after transformation of phosphate polyanion structure. It implies that capable of delivering the improved electrochemical properties than no possessed by substituted materials.<sup>35-39</sup> Therefore, Fluorine substitution at the oxygen site of the cathode active materials for lithium ion batteries attracts much attention in recent years. Many researchers had pursued the fact that the substitution of oxygen by fluorine was an attractive strategy to improve electrochemical performance.<sup>40-44</sup> It is reported that the fluorine substitution is effective to improve cycling life for layered structure cathode materials. The crystal structure of these materials was stabilized by partially substituting fluorine for oxygen, and the phase transitions during charge and discharge are partially suppressed. Furthermore, fluorine substitution catalyzes the growth of the primary particles, which in turn results in high tap density as well as high volumetric capacity.<sup>45, 46</sup>

In this study, fluorine anion substitution was attempted to overcome the inherent disadvantages and to achieve improved electrochemical performance. A small amount of fluorine doping improves conductivity, stabilizes the structure, and positively affects electrochemical performance.<sup>47</sup>

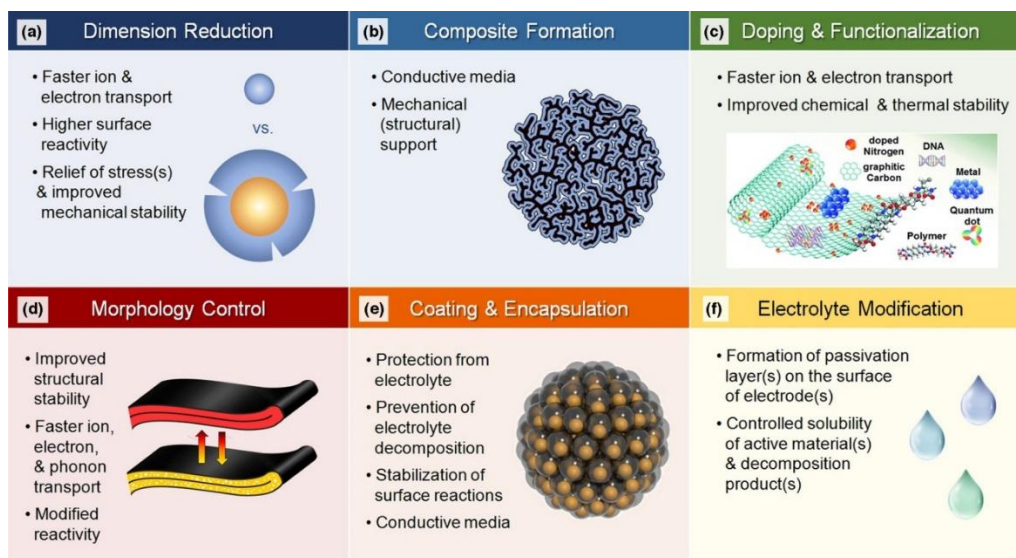


**Figure 1.9** General strategies for performance enhancement and their rationale: (a) reducing dimensions of active materials, (b) formation of composites, (c) doping and functionalization, (d) tuning particle morphology, (e) formation of coatings or shells around active materials, (f) modification of electrolyte.<sup>34</sup>

## 2. Introduction of Nuclear Magnetic Resonance (NMR)

### 2.1 The principle of NMR

Nuclear magnetic resonance (NMR) spectroscopy is basically a type of absorption spectroscopy. The NMR measurement is absorbing radiofrequency (RF) radiation energy specific to the nucleus in placed in a strong magnetic field. Upon absorption under certain conditions, the nuclei begin to resonate and different atoms within a molecule resonate at different frequencies. RF waves are low-energy electromagnetic radiation with frequencies from several kHz to several hundred GHz. The energy of RF wave radiation is insufficient to cause vibrations, rotations or electron excitation of atom or molecules but it is enough to affect atomic nuclear spins, which allow a detailed analysis of the molecular structure..<sup>48</sup>

The Nucleus has with spin angular momentum that is quantized in size and direction. To perform NMR analysis, the nuclear spin quantum number ( $I$ ) should not be zero and have magnetic moment ( $\mu$ ). In case of nuclei with odd numbers of both protons and neutrons have spin quantum numbers that are positive integers. The remaining nuclei all have spins that are half integral. Nuclei containing even numbers of both protons and neutrons have  $I=0$  and therefore cannot undergo NMR. (<sup>12</sup>C, <sup>16</sup>O etc.) But, every element in the periodic table has at least one isotope that can experience NMR that is NMR active when placed in a magnetic field. The different nuclear spin quantum number for the nuclide is shown in Figure 2.1.

The nuclear spins are tiny compass needles that, under the influence of the external magnetic field, are aligned causing a net magnetic moment to build up along the  $B_0$  direction, which is commonly defined to be the  $z$  direction (Figure 2.2a, b). Nuclear spin states must be quantized to observe the resonance phenomenon of nuclear spins. That is, the energy level

should be separated. The number of spin states has  $2I+1$ . When active spins are placed in a strong magnetic field, it aligns them according to their energy state, which is called the Zeeman Effect. The arrangement of nuclear spins can be aligned in the same or opposite direction as the magnetic field. These two nuclear spin alignments have different energies, and these energy differences are related to the Larmor frequency. In case of  $^1\text{H}$  nucleus, it has two energy state since its nuclear spin quantum number is  $1/2$  ( $I = 1/2$ ). Figure 2.3 illustrates that Zeeman Effect.<sup>49, 50</sup>

Absorption of the radiation causes the nuclear spin to realign or flip in the higher-energy direction. After absorbing energy, the nuclei will re-emit RF radiation and return to the lower-energy state. This process involves the thermal equilibrium of magnetization the thermal equilibrium of longitudinal magnetization is manipulated by RF pulses, which are applied on the sample through an RF coil used for both manipulation of the spin system and signal detection. The net magnetization is thereby transferred into the x-y plane (transverse magnetization), where it rotates around the z axis. This rotation of the magnetic moment inside the coil induces a voltage. Because of internal NMR interactions and so-called spin-spin relaxation processes ( $T_2$  relaxation), a relatively quick loss of this coherency occurs as well as a slow recovery to the longitudinal magnetization. This causes a decay of the induced voltage, which is measured as the free induction decay (FID). FID signals are transformed by Fourier transformation (FT), which the voltage-time signal is translated into an intensity-frequency signal (Figure 2.4).<sup>51</sup>



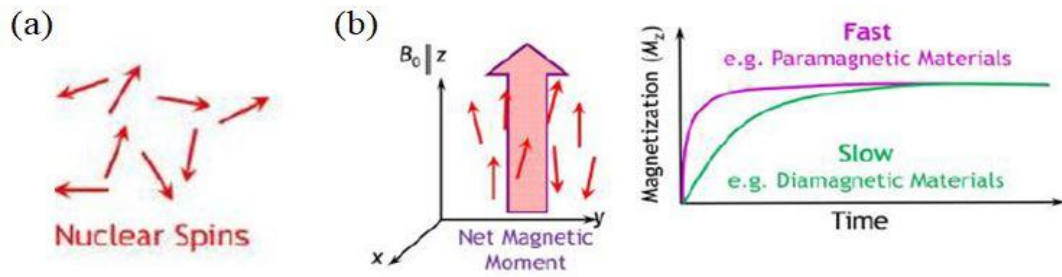


**Figure 2.2** (a) No magnetization is present for the randomly orientated nuclear spins of the sample. (b) Longitudinal magnetization along the z-axis builds up as soon as a magnetic field  $B_0$  is applied. A net magnetic moment results.<sup>51</sup>

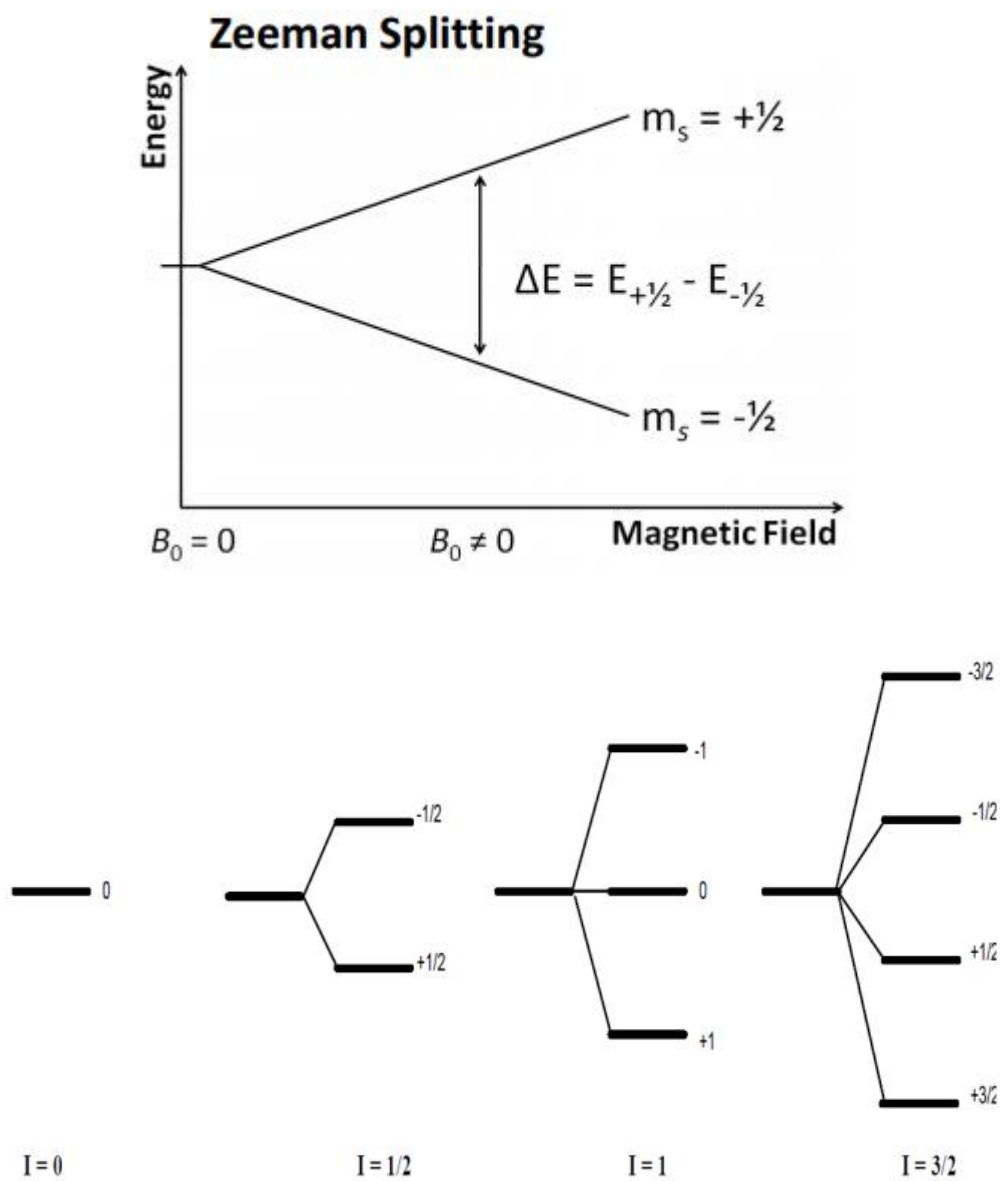


**Figure 2.3** Illustration of Zeeman Splitting of Energy levels.<sup>50, 53</sup>

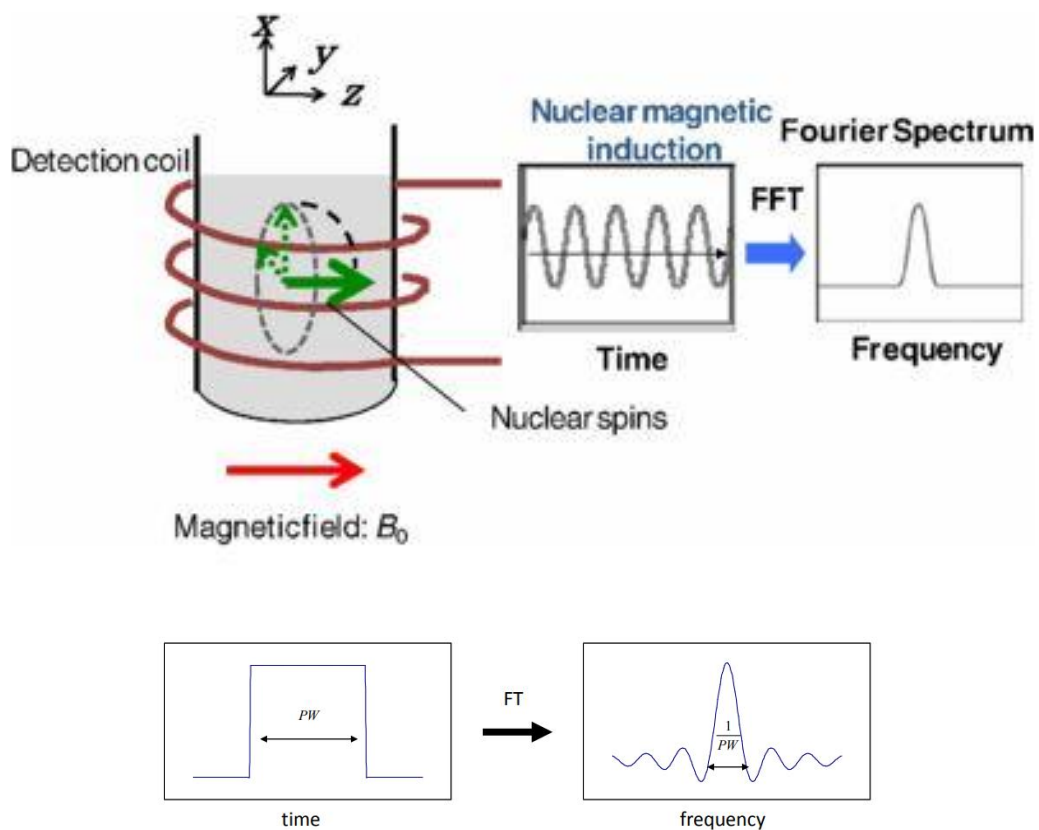


**Figure 2.4** Schematic illustration of the operation principle of conventional NMR.<sup>50, 54</sup>

### 2.1.1 Boltzmann distribution

When there is no external magnetic field, the nuclear spins are randomly oriented in any direction, but when a magnetic field ( $B_0$ ) is applied, the nuclear spins are oriented in the same direction or in opposite directions. Therefore, energy becomes different. Spins in the same direction as the magnetic field ( $B_0$ ) are more stable and exist in lower energy state ( $\alpha$ ) and spins in the opposite direction are in a higher energy state ( $\beta$ ). The number of nuclei in each spin state can be described by the Boltzmann distribution equation demonstrated in Equation 2.1. The Boltzmann equation expresses the relationship between temperature and the related energy as shown below.

$$\frac{N_\alpha}{N_\beta} = e^{-\Delta E/kT} \quad (2.1)$$

Where  $N_\alpha$  is the number of spins in the higher energy state,  $N_\beta$  is the number of spins in the lower energy state,  $k$  is Boltzmann's constant ( $1.3804 \times 10^{-23} \text{ J K}^{-1}$ ),  $T$  is the absolute temperature.

$$\Delta E = h\nu = \frac{\gamma h}{2\pi} B_0 \quad (2.2)$$

Substituting Equation 2.2 into Equation 2.1 gives

$$\frac{N_{\alpha}}{N_{\beta}} = e^{-\left(\frac{\gamma h B_0}{2\pi k T}\right)} \quad (2.3)$$

Where  $N_{\alpha}$  and  $N_{\beta}$  represent the population of nuclei in higher and lower energy states,  $E$  is the energy difference between the two spin states,  $k$  is the Boltzmann constant ( $1.3805 \times 10^{-23} \text{ J} \cdot \text{K}^{-1}$ ) and  $T$  is the temperature in K,  $h$  is plank's constant ( $6.626 \times 10^{-34} \text{ J} \cdot \text{s}$ ). At room temperature, the number of spins in the lower energy level is  $N$  lower whereas the number in the upper level is  $N$  upper. Spins of the nucleus with a low energy state can be excited to a higher energy state by irradiating the nucleus with electromagnetic radiation of the correct energy. The absorption of energy occurs during this transition<sup>55</sup>

### 2.1.2 T<sub>1</sub> (Spin-lattice relaxation) and T<sub>2</sub> (Spin-spin relaxation)

In NMR, a magnetic field generated by flowing an alternating current to a coil at a radio frequency is called the B<sub>1</sub> magnetic field. When the alternating current flowing into the coil is turned on and off, a pulse B<sub>1</sub> magnetic field is generated. The spin of the nucleus is aligned in the same or opposite direction to the external magnetic field along the z-axis. Since there are many nuclei oriented in the same direction as the magnetic field, net magnetization exists parallel to the external magnetic field.

At this time, the nucleus spin of the z-axis can be inverted to the x-y plane by injecting a short pulse. After the pulse injection, the spin system tries to return to the equilibrium state, and the time taken for this is called the relaxation time. The relaxation time is divided into T<sub>1</sub> (Spin-lattice relaxation time) and T<sub>2</sub> (Spin-spin relaxation time) which indicates how fast the nucleus spins are magnetized in the z-axis. At equilibrium state, the net magnetization vector lies in the same direction as the external magnetic field (B<sub>0</sub>) is called equilibrium magnetization (M<sub>0</sub>).

When energy is applied to the system, the spin system is saturated and M<sub>z</sub> becomes zero (M<sub>z</sub> = 0). In this saturation state, the time that it takes for M<sub>z</sub> to return to its original equilibrium state is called T<sub>1</sub> (spin-lattice relaxation time) and is expressed with the following equation and expressed as figure 2.5.

$$M_z = M_0(1 - e^{-t/T_1}) \quad (2.4)$$

When the net magnetization lies in the x-y plane by a pulse, it rotates about the z-axis at the Larmor frequency. The spinning motion is called precession. Precession and net magnetization experience slightly different magnetic fields in each spin, and eventually

rotate at different Larmor frequencies and de-phasing begins to occur. As a result, a larger de-phasing occurs over time. The time required for the transverse magnetization  $M_{xy}$  to return to the equilibrium state is referred to as  $T_2$  (spin-spin relaxation time) and is represented by the following equation and expressed in figure 2.6.

$$M_{xy} = M_{xy0} e^{-t/T_2} \quad (2.5)$$

That is,  $T_1$  is the time for how fast the nuclear spins are magnetized in the z-axis,  $T_2$  is how fast the magnetization is lost in the x-y plane, and  $T_2$  is equal to or less than  $T_1$ .

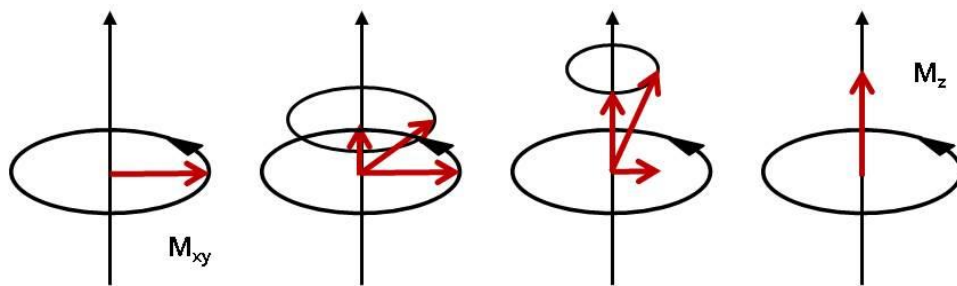
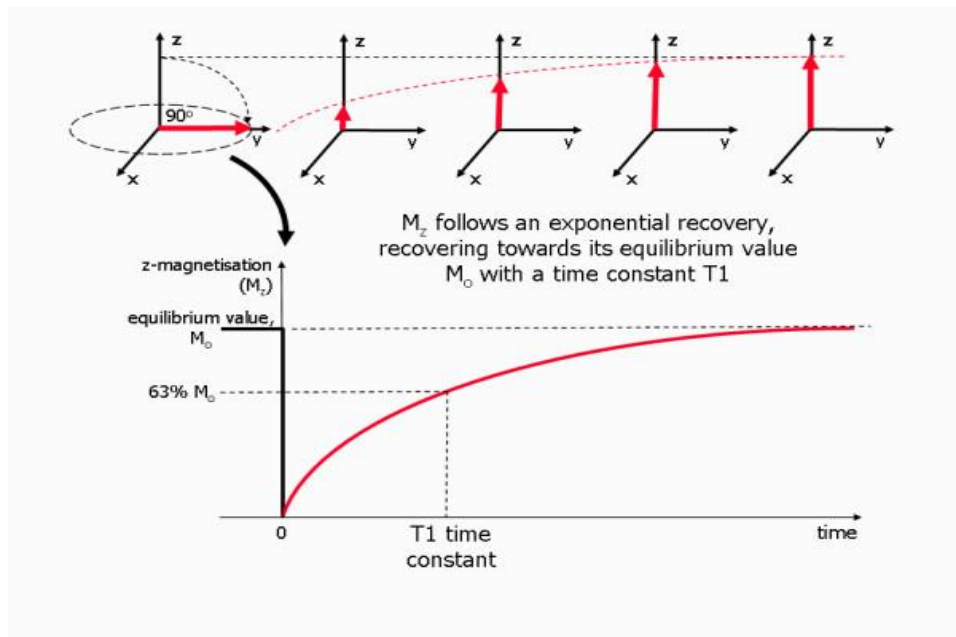
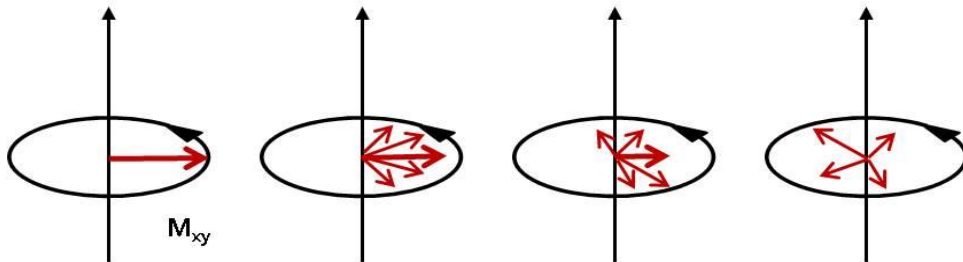
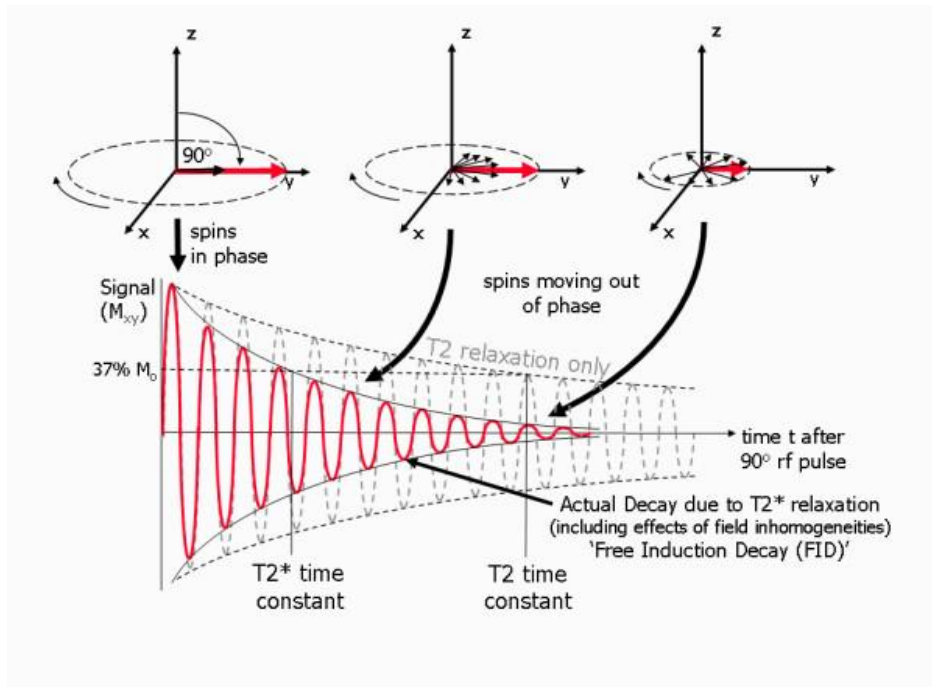


Figure 2.5 Spin-lattice relaxation ( $T_1$ ) processes<sup>56</sup>



**Figure 2.6** Transverse ( $T_2$  and  $T_2^*$ ) relaxation processes<sup>56</sup>

## 2.2 Solid-state NMR

Since the NMR spectrum arising from nuclear spins in a powder sample often spans a very large frequency range, instruments for solids are mechanically equipped with high-speed digitizers that can provide faster sampling rates compared to spectrometers designed specifically to examine liquids. In contrast to liquid samples that can use low power RF pulses, solid samples can detect spin interaction using a high-power RF pulse. It requires a large power capacity of the radio wave transmitter to provide short and strong pulses due to short spin-spin relaxation time. Also, it can analyze the physical properties of the sample, but it exhibits a broad spectrum due to the chemical shift anisotropy (CSA), dipole-dipole coupling and quadrupolar coupling. The effect of broadening according to sample type is demonstrated in Figure 2.7.

In the case of solid NMR, the specimen is placed into a ceramic type rotor, which is different from those of liquid NMR tube, and the sample is measured rotating at  $\sim$  kHz or without rotating the sample in a stationary state. Especially, in the case of single crystal samples, the change of resonant frequency is observed and analyzed according to the relative direction to the magnetic field. In addition, the analysis of the spectrum shape of a fine powder state or lump composed of innumerable domains allow to obtain information on structure and dynamics.

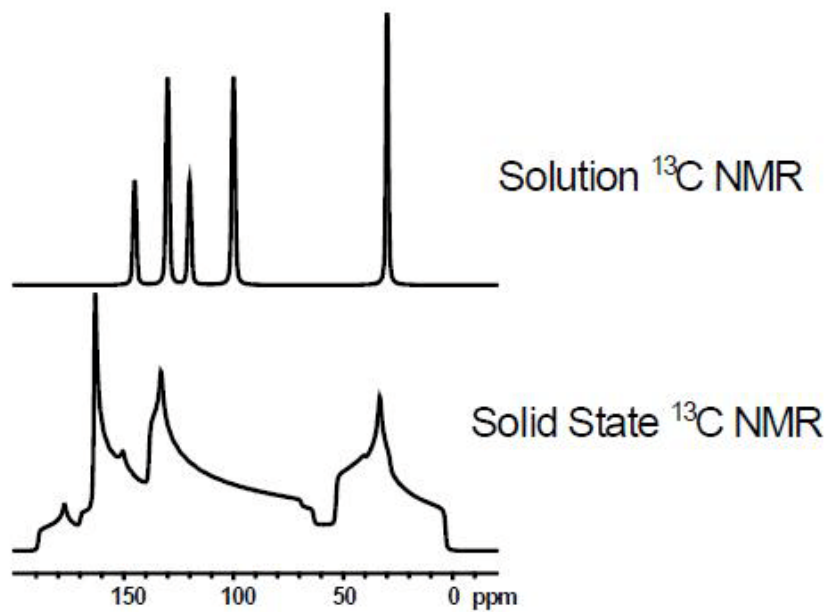


**Figure 2.7** Comparison between spectra of solution  $^{13}\text{C}$  NMR and solid state  $^{13}\text{C}$  NMR.<sup>57</sup>

### 2.2.1 Interaction-type in Solid-state NMR

The external magnetic field  $B_0$  induces currents of the electrons surrounding the nucleus, which in turn create local magnetic fields that lead to shielding the nucleus. Consequently, characteristic changes in nuclear resonance frequency are obtained. The electron distribution around the nucleus is asymmetric and the shielding effect depends on the orientation of the molecules under the influence of the magnetic field  $B_0$ . This is called chemical shift anisotropy and the resonance frequency depends on the orientation of chemical shift tensor that is affected with magnetic field. Nuclear spins exhibit a dipole moment that interacts with the dipole moment of other nuclei known as dipole coupling. The intensity of the interaction is related in the spin species, the internuclear distance, and the orientation of the vector connecting the two nuclear spins with the external magnetic field  $B_0$ . Also, an atomic nucleus with spin greater than 1 is split by the uneven electric field due to the quadrupole moment and energy separation by quadrupole moments does not occur in the solution state due to the symmetry. Thus, quadrupole interaction is observed only in solid-state.<sup>55</sup>

### 2.2.2 Magic Angle Spinning (MAS) technique

MAS NMR is a technique for obtaining high resolution NMR data from solids. Contrary to solution NMR, where anisotropic interactions are averaged by the rapid tumbling of molecules, in solid-state NMR, interactions such as the chemical shift anisotropy (CAS) and dipolar coupling dominate. As a consequence, the spectral line width of nuclei in solids is rather broad.<sup>58</sup> In order to overcome this problem in the solid state, the MAS technique, known since the 1950s, is usually employed.

The chemical shift interaction is called the chemical shift anisotropy because of the anisotropy of the electronic environment that varies depending on the direction, which is caused by the surrounding electrons that modify the local environment of the nucleus. Another type of interaction is dipolar interaction that occurs by direct spatial coupling between nuclei. At last but not least, quadrupole interaction caused by the interaction between electric quadrupole moment of the nuclei and the asymmetric electric field gradients surrounding the nucleus and this type of interaction occurs when the nuclear spin  $I$  is greater than  $\frac{1}{2}$ . These three interactions include in the term of  $3\cos^2\theta - 1$  and when they are removed, sharp peaks appear. This technique is called Magic Angle Spinning (MAS) and the expression for the term to be 0 is as follows.

$$(3\cos^2\theta - 1) = 0, \theta = 54.74^\circ$$

And, the sample must be spin around an axis that is oriented at an angle  $54.74^\circ$  to the magnetic field  $B_0$ . Figure 2.8 and Figure 2.9 are schematic representation of the MAS experimental effect. The spinning speed must be faster than the interaction strength to average out the anisotropy.

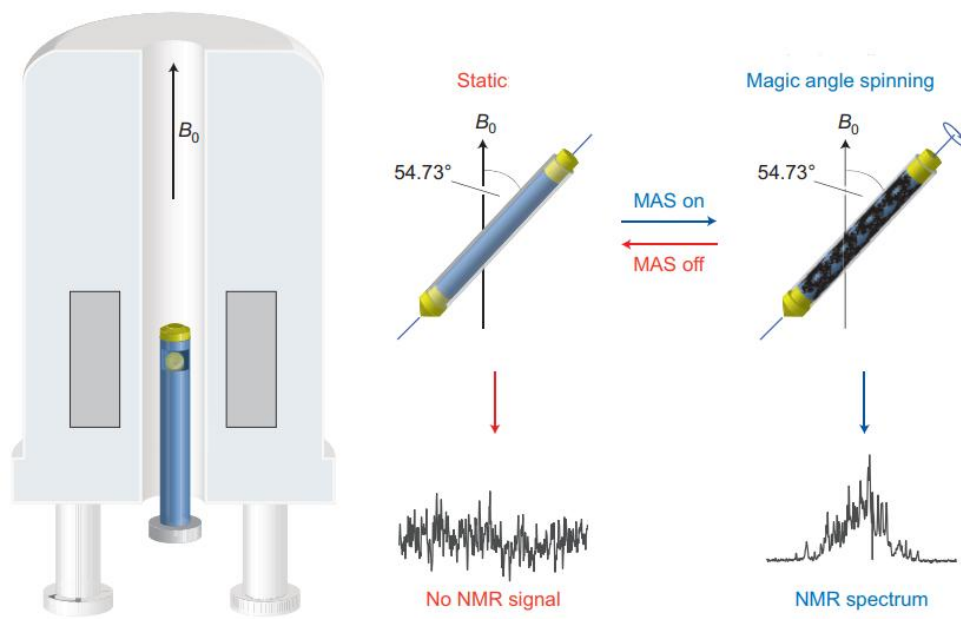


**Figure 2.8** A schematic representation of a transient sedimentation NMR experiment<sup>59</sup>

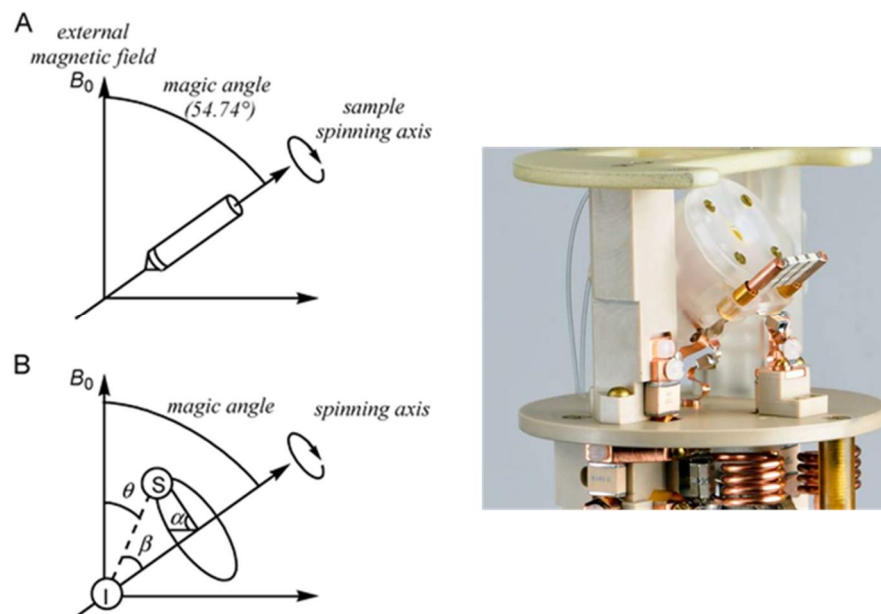


**Figure 2.9** Illustration of magic angle spinning (MAS). (a) A pair of nuclear spins I and S in the solid-state NMR sample tube rotate along the axis tilted magic angle ( $54.741^\circ$ ) with respect to the external magnetic field. (b) Rotation of the I–S internuclear vector under MAS is expressed by angles  $\alpha$  (azimuth angle; rotation of I–S vector around the spinning axis) and  $\beta$  (polar angle; tilt angle between the I–S vector and spinning axis)<sup>60, 61</sup>

### 2.2.3 Spin echo pulse sequence (Hahn echo)

A pulse sequence is a set of pulses applied to a sample to produce a specific form of NMR signal. Parameters of spectrometer frequency, pulse width (pw), recycle delay (d1) and acquisition time (aq) are important for obtaining NMR signals. The spectrometer frequency is a specific frequency of propagation pulses that depends on the strength of the magnetic field and the type of nuclei to be measured. A radio pulse excites a relaxing nucleus while acquiring a signal. The signal is obtained by decreasing the dephasing after the net magnetization vector carries out a precession about the z-axis. At this time, a sine curve is obtained with exponential decay, which is called free induction decay (FID). The recycle delay (d1) is the time it takes for the spin to fully magnetize on the z axis, which appears at the beginning of the pulse sequence and is also known as the delay time. After the pulse is applied, the nuclear spin does not immediately return to equilibrium and relaxes with a time constant T1. This depends on factors such as the nuclear environment, temperature, solvent and other magnetic field conditions.<sup>62</sup> The pulse sequence of 1D NMR is shown as Figure 2.10.

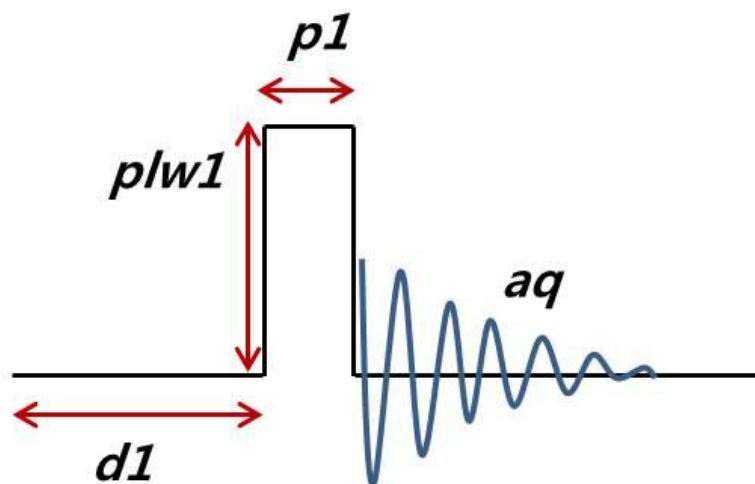


**Figure 2.10** Schematic illustration of 1D NMR pulse sequence. ( $p1$  = pulse width or duration,  $plw1$  = RF field strength,  $aq$  = acquisition time and  $d1$  = delay time)

We are mainly interested in relaxation, but there are other effects that contribute to the decay in the FID like inhomogeneity in the magnetic field. Dephasing caused by T2 relaxation is a random irreversible process. A global inhomogeneity of the static magnetic field  $B_0$  causes parts of the sample to precess at different rates so that the phase differences and a loss of the ensemble-averaged transverse magnetization can occur much faster than expected from just spin-spin interactions alone. Fortunately, however, the effect of field inhomogeneity like additional dephasing is potentially reversible.<sup>56</sup>

Even after the FID has decayed, it is possible to recover the transverse magnetization from the relaxation up to the amount lost irreversibly. This recovery concept was discovered by Erwin Hahn in 1950 and is known as a spin echo.<sup>63</sup> It is the foundation of a wide range of pulse sequences. Commonly, Spin echo is generated by applying a  $180^\circ$  refocusing RF pulse after a  $90^\circ$  excitation pulse. Thereby, the  $90^\circ$  pulse is called excitation pulse and  $180^\circ$  pulse is refocusing pulse.<sup>61</sup> Spin echo, as opposed to FIDs, can be produced using two RF pulses in succession. Echo can be used to overcome dead time limitations, which are often encountered in observation of resonances from solid state materials. The echo pulse sequence consists of two RF pulses:  $\pi/2$  and  $\pi$  respectively or two  $\pi/2$  pulses (i.e. solid echo, useful when observing quadrupolar nuclei), separated by a delay  $\tau$  as in the Figure 2.11.

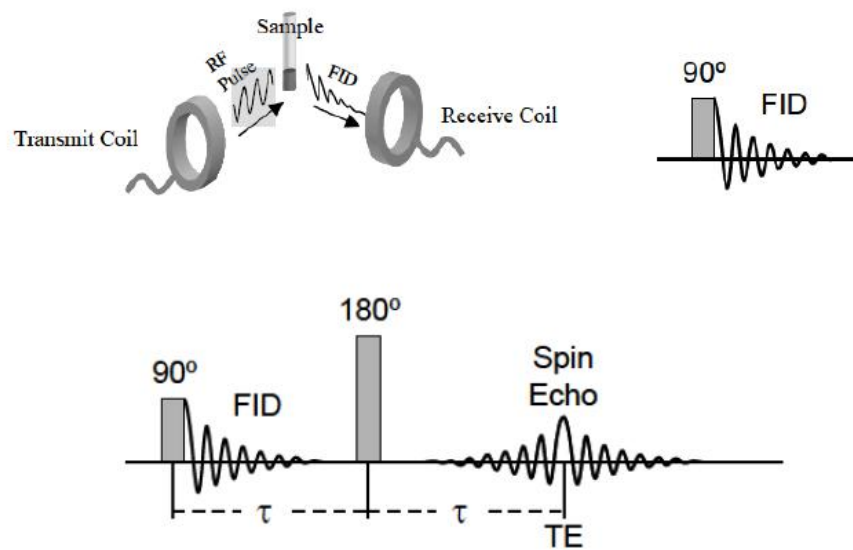


**Figure 2.11** Representation of spin echo sequence. The NMR signal is measured according to the initial excitation pulse attenuation.

## 2.2.4 Structural analysis using NMR for cathode materials

The NMR analysis of battery cathode materials not only provide information about the signal shifts of the other chemical species of the material but also enables the study of the interfaces of the electrochemical cells. Solid-state NMR spectroscopy, especially when investigating battery materials, offers a huge database in which to gather this information. Chemical and electrochemical processes rely on redox reactions. Ions such as Li<sup>+</sup> and Na<sup>+</sup> are often directly involved in this process and the <sup>6</sup>Li, <sup>7</sup>Li and <sup>23</sup>Na NMR spectra are affected by the electronic structure of the material under investigation, respectively. In addition, the range of nuclei that can be used to gain insight into electronic and structural changes in matter is not limited to <sup>6</sup>Li, <sup>7</sup>Li and <sup>23</sup>Na. Many other nuclei, for example, I=1/2 isotopes like <sup>1</sup>H, <sup>13</sup>C, <sup>19</sup>F, and <sup>31</sup>P as well as quadrupolar nuclei with I>1/2 like <sup>2</sup>H, <sup>17</sup>O, <sup>25</sup>Mg, <sup>27</sup>Al, <sup>33</sup>S, and <sup>51</sup>V, can provide useful insights. In combination with diffraction methods, complementary information on both crystal and electronic structure are accessible. Furthermore, NMR can be used to derive information on ion dynamics, e.g., activation energies, which can be correlated with data from theoretical calculations as well as other experimental techniques.<sup>49</sup> The various nuclei guide is represented in Table 2.1

**Table 2.1** Short Guide to Accessible Nuclei for Different Types of Energy Storage Materials<sup>51</sup>

Isotope	Spin	N.A. (%)	Q (fm <sup>2</sup> )	F.R. (%)	Major challenges	Information and materials' applications
<sup>1</sup> H	1/2	99.99		100.00	Signal background	Electrolytes, supercapacitors, surface chemistry
<sup>13</sup> C	1/2	1.07		25.25	Low N.A. (enrichment); partial enrichment allows detection of specific functional groups	Electrolytes, supercapacitors, carbon anodes, SEI
<sup>19</sup> F	1/2	100		94.09	Signal background	Electrolytes, supercapacitors, cathode coatings, SEI
<sup>29</sup> Si	1/2	4.68		19.87	Low N.A. (enrichment)	Si anodes
<sup>31</sup> P	1/2	100		40.48	Slow relaxation can cause long experiment times	Phosphide and phosphate electrodes, electrolytes, SEI
<sup>119</sup> Sn	1/2	8.59		37.29	Comparably low N.A.	Sn metal anodes
<sup>2</sup> H	1	0.01	0.29	15.35	Low N.A. (enrichment)	See <sup>1</sup> H for applications; better suited to study dynamics
<sup>6</sup> Li	1	7.59	-0.08	14.72	Low N.A. (enrichment)	See <sup>7</sup> Li for applications; improved resolution vs <sup>7</sup> Li (smaller quadrupolar and dipolar broadening); provides some complementary information when combined with <sup>7</sup> Li
<sup>7</sup> Li	3/2	92.41	-4.01	38.86	Comparably small diamagnetic shift range	Electrolytes, electrodes, dynamics, SEI
<sup>17</sup> O	5/2	0.04	-2.56	13.56	Low N.A. (enrichment); enrichment readily available but expensive	Metal-air batteries, oxygen dynamics in oxide materials
<sup>23</sup> Na	3/2	100	10.4	26.45	None	Electrolytes, electrodes, dynamics, SEI
<sup>25</sup> Mg	5/2	10.00	19.94	6.12	Low FR, low N.A., large quadrupole moment; low sensitivity without expensive enrichment	Beyond Li-ion technologies: divalent Mg <sup>2+</sup>
<sup>27</sup> Al	5/2	100	14.66	26.06	Large quadrupole moment	Beyond Li-ion technologies: trivalent Al <sup>3+</sup> ; cathode coatings, solid electrolytes
<sup>33</sup> S	3/2	0.76	-6.78	7.68	Low N.A. (enrichment); expensive enrichment; very broad signals	Li-S, all-solid-state batteries
<sup>39</sup> K	3/2	93.26	5.85	4.67	Low sensitivity and long relaxation times	Beyond Li-ion technologies: K <sup>+</sup>
<sup>43</sup> Ca	7/2	0.135	-4.08	6.73	Requires very expensive enrichment	Beyond Li-ion technologies: divalent Ca <sup>2+</sup>
<sup>51</sup> V	7/2	99.75	-5.2	26.30	Large quadrupole moment	Electrodes; redox flow batteries
<sup>67</sup> Zn	5/2	4.10	15.9	6.26	Very large quadrupole moment; expensive enrichment	Zn-air batteries, redox flow batteries

<sup>a</sup>Isotopes, nuclear spin (*I*), natural abundance (N.A.), quadrupole moment (*Q*), and frequency ratio (F.R., relative to <sup>1</sup>H) are given and some major experimental challenges as well as selected applications summarized.

### 3. Experimental

#### 3.1 Synthesis

The solid-state reaction is the most common method to prepare ceramics, in which solid precursors are ball-milled together, followed by heat-treatment in a furnace. In the case of monoclinic  $\text{Li}_2\text{FeP}_2\text{O}_7$ , the raw material involves not only lithium (e.g.,  $\text{LiH}_2\text{PO}_4$ ,  $\text{Li}_2\text{CO}_3$ ,  $\text{LiOH}$ , and  $\text{LiF}$ ), iron (e.g.,  $\text{FeC}_2\text{O}_4 \cdot 2\text{H}_2\text{O}$ ), and phosphorous (e.g.,  $\text{NH}_4\text{H}_2\text{PO}_4$  or  $(\text{NH}_4)_2\text{HPO}_4$ ) sources, but also carbon-containing (e.g., Ketjen Black) or organic compounds (e.g., glucose).<sup>18, 64</sup>

In this study, fluorine-substituted  $\text{Li}_2\text{FeP}_2\text{O}_{7-x}\text{F}_{2x}$  ( $x = 0, 0.005, 0.01, 0.03, 0.05, 0.10, 0.05$  and  $1.00$ ) without additional carbon sources as a cathode material for lithium rechargeable batteries were prepared via solid-state reaction. Stoichiometric amounts of  $\text{Li}_2\text{CO}_3$  (Aldrich,  $\geq 99\%$ ),  $\text{FeC}_2\text{O}_4 \cdot 2\text{H}_2\text{O}$  (Junsei,  $\geq 99\%$ ),  $(\text{NH}_4)_2\text{HPO}_4$  (Junsei,  $\geq 99\%$ ), and  $\text{LiF}$  (Wako,  $\geq 98\%$ ) as a substitution reagent were used. Stoichiometric amounts of the reactants in acetone media were planetary milled with zirconia balls for 2 h at 300 rpm and dried in an oven at  $80\text{ }^\circ\text{C}$  for approximately 12 h, and ground using a mortar and pestle. The obtained precursor powder was purged to prevent oxidation in a tube furnace under pure argon gas for 5 h and first sintered at  $350\text{ }^\circ\text{C}$  for 3 h due to organic partly decomposing and subsequently sintered at  $600\text{ }^\circ\text{C}$  for 12 h. It is heated at a rate of  $5\text{ }^\circ\text{C min}^{-1}$  and finally cooled to room temperature. This scheme process is shown in the Figure 3.1.

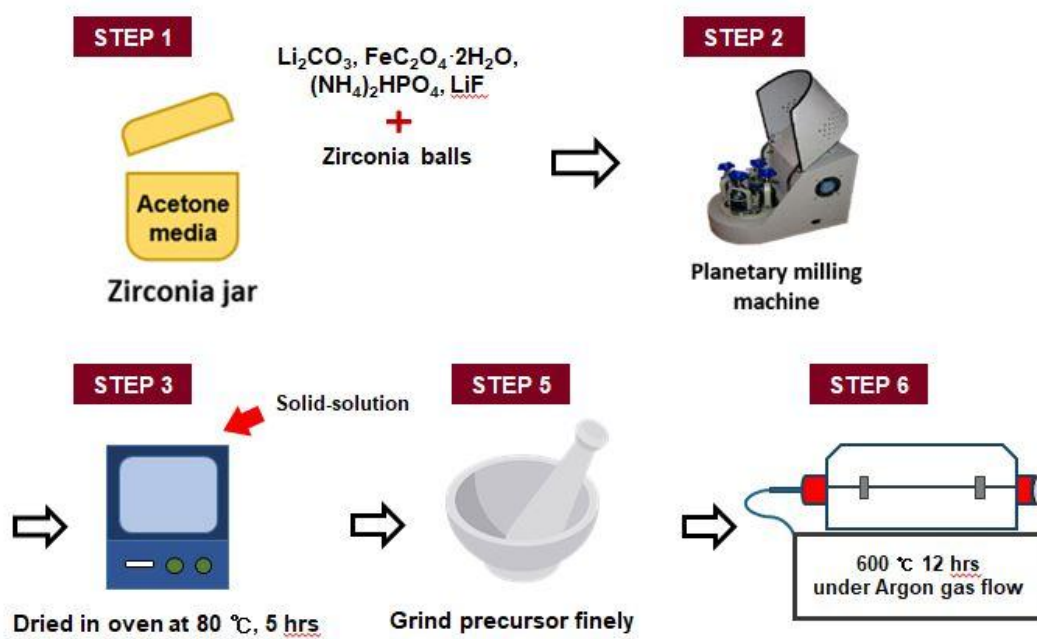


**Figure 3.1** Solid-state synthetic procedures of  $\text{Li}_2\text{FeP}_2\text{O}_{7-x}\text{F}_{2x}$  as a cathode material.

### 3.2 General characterization

A thermo gravimetric analysis and simultaneous differential scanning calorimetry (TG/DSC, SDT Q600 V20.9 Build 20, TA Instruments) were performed to evaluate endothermic and exothermic processes such as pyrolysis, decomposition, and crystallization of precursors in the model system. The samples used for this analysis were the  $\text{Li}_2\text{FeP}_2\text{O}_7$  precursors. The analysis was performed at a heating rate of  $10\text{ }^\circ\text{C min}^{-1}$  in the temperature range of 25 - 900 under  $\text{N}_2$  atmosphere. The evolution of crystalline phases as a function of heating temperature was studied using X-ray diffraction (XRD, Rigaku Ultima 4, Japan) with  $\text{Cu K}\alpha$  radiation ( $\lambda = 1.5406\text{ \AA}$ ). The operating conditions of the XRD were 50 kV and 40 mA over the  $2\theta$  range of between 10 and  $50^\circ$  at a step size of  $0.01^\circ$  in continuous scan mode at  $2^\circ\text{ min}^{-1}$ . ICSD provided by FIZ Karlsruhe was used to identify the phases in the samples. The surface morphology and grain sizes of sintered active material were identified by Schottky-type field emission scanning electron microscopy (FE-SEM, JSM-7610F, JEOL, Japan) equipped with an energy dispersive spectrometer (EDS, X-Max, Oxford Instruments, England). The sample was adsorbed onto a mount with carbon tape and a Pt coating was performed using a CRESSINGTON SPUTTER COATER 108 auto at 10 mA during 30 s to prevent the charging reaction. Measurements were performed at an accelerating voltage of 10 kV, WD 8.0 mm and a probe current of 10 nA. Also, Transmission electron microscope (TEM) was acquired by Hitachi H-8100 and JEM-1400 with accelerating voltage of 200 kV and 120 kV, respectively. A CCD camera was used to acquire TEM images and selected area electron diffraction (SAED) patterns. The sample was pipetted, and a drop was placed onto a TEM grid covered with a lacey carbon film at room temperature and then blotted with filter paper for 1 s before plunging. Afterwards, the grids were kept in liquid nitrogen, transferred to a cryo-holder, inserted into a microscope and observed in a frozen state. Ultrafast freezing

transforms water into a vitreous state and allows the observation of the embedded products of the reaction in their original state. The X-ray photoelectron spectroscopy (XPS) measurements were performed by using PHI 5000 Versa Probe (Ulvac-PHI, Japan) analyzer at base pressure =  $2.0 \times 10^{-7}$  Pa. Al K $\alpha$  (1486.6 eV) radiation was used as an excitation source. The data was made by using XPSpeak41 software and subtracted background was of “Shirley” type.

### 3.3 Electrochemical test

The electrochemical measurements were conducted using CR 2016 typed coin cells. The coin cells were comprised of the cathode electrode (working electrode), metallic Li foil as the anode electrode, electrolyte, and separator. To prepare the working electrode, a mixture of 80 wt.% active material (synthesized cathode material), 10 wt.% conductive material (super-P) and 10 wt.% poly(vinylidene fluoride) (PVDF, Aldrich, Mw = 534,000) was mixed in *N*-methyl-2-pyrrolidone (NMP) until viscosity slurry. The obtained slurries were pasted onto an aluminum foil substrate (thickness 15  $\mu\text{m}$ ) using a doctor blade and followed by drying in a vacuum oven at 80  $^{\circ}\text{C}$  for 2 h. After that, they were squeezed using a roll press for uniformity of the electrode thickness. And then, the electrodes were punched to a diameter of 15 mm and the cells were assembled into 2016-coin cells in an argon-filled glove box. The amount loaded on the 15 mm diameter cathode material was approximately 4 to 5 mg. Lithium metal foil, 15 mm in diameter and 0.30 mm in thickness, was used as the counter electrode. Cellgard-2400 porous polypropylene was used as a separator. Non-aqueous 1.0 M  $\text{LiPF}_6$  in EC/DMC (ethylene carbonate/dimethyl carbonate) with 1: 1 volume ratio was used as the electrolyte.

The electrochemical cycle tests and cyclic voltammetry (CV) were performed at ambient temperature using a galvanostatic automatic battery cycler (WonATech WBCS3000, Korea). The cells for rate test were cycled between 2.0 and 4.3 V vs.  $\text{Li}/\text{Li}^+$  using a constant current-constant voltage (CC-CV) protocol in charging mode. The constant current rates were 0.05, 0.1, 0.2, 0.5, 1 and 2 C at 4.3 V and kept at 4.3 V until the current rate decreased to C/20 with a constant current density of 110  $\text{mAh g}^{-1}$  for the 1 C rate. And, CV were performed at a scan rate of 0.05  $\text{mV s}^{-1}$ .

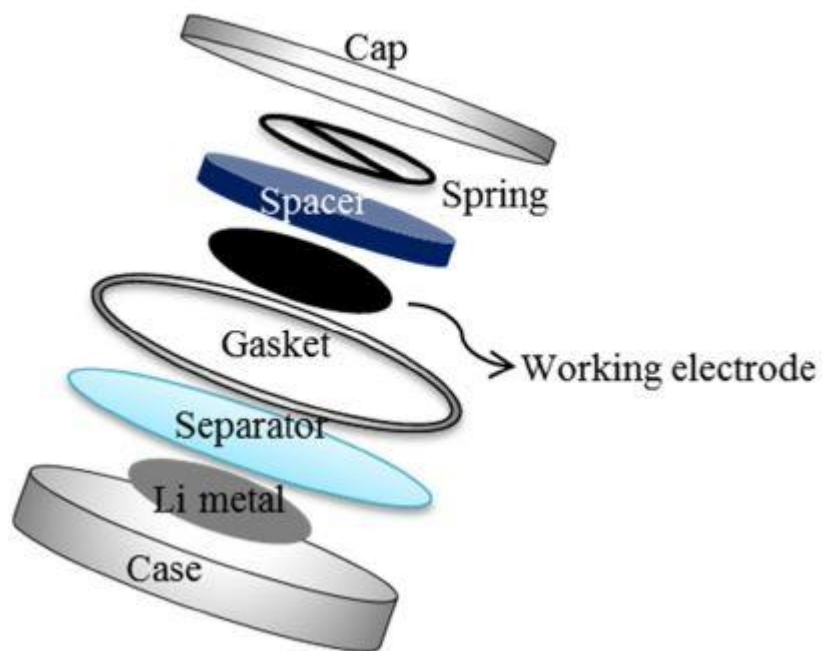


**Figure 3.2** Illustration of a coin cell type assembly.

### 3.4 Solid-state MAS NMR study of cathode materials

$^7\text{Li}$  and  $^{31}\text{P}$  Magic angle spinning (MAS) nuclear magnetic resonance (NMR) measurements were carried out at room temperature on a Bruker Avance III 300 with a 7.04 T magnet. For the MAS NMR experiments, a 2.5 mm MAS probe was used with a zirconia rotor at 116.64 MHz for  $^7\text{Li}$  and 121.49 MHz for a  $^{31}\text{P}$  resonance frequency. The  $^7\text{Li}$  NMR spectrum was referenced to the external LiCl powder and  $^{31}\text{P}$  NMR spectrum to the 85%  $\text{H}_3\text{PO}_4$  (aq) reference. The Hahn-echo pulse sequences for  $^7\text{Li}$  and  $^{31}\text{P}$  were used to observe the NMR signal and the sample spinning rate was 25 kHz, 30 kHz about each  $^7\text{Li}$  and  $^{31}\text{P}$ . The  $^7\text{Li}$  spectra were acquired with a  $90^\circ$  pulse length of 2.0  $\mu\text{s}$ , repetition delay of 0.5 s, 1K transients, and a spectral width of 0.23 MHz. For  $^{31}\text{P}$  NMR, the  $90^\circ$  pulse length of 2.0  $\mu\text{s}$ , repetition delay of 0.5 s, and 4K transients with a spectral width of 0.60 MHz were used. The isotropic chemical shifts were successfully identified by varying the sample spinning rates.



**Figure 3.3** Bruker Avance III 300MHz NMR.

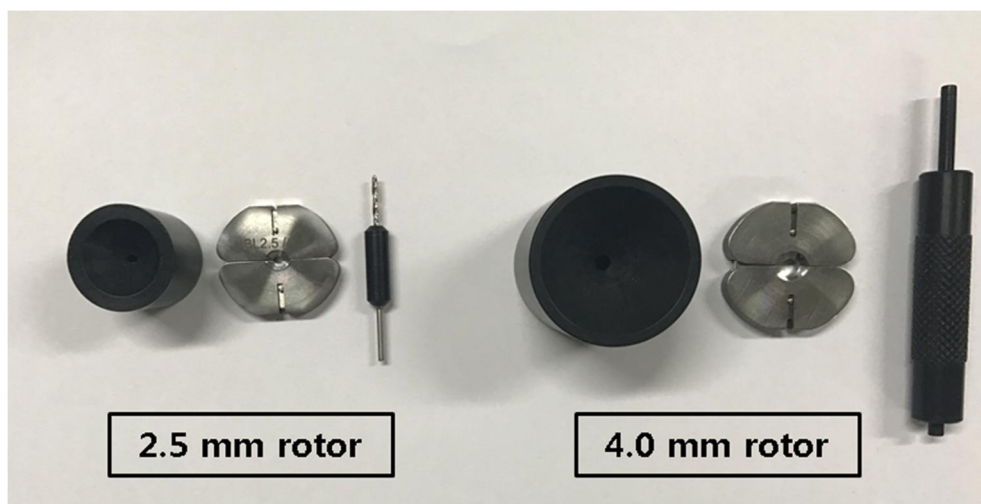


**Figure 3.4** Sampling kit for solid-state NMR.



**Figure 3.5** Solid-state NMR rotor of various sizes<sup>65</sup>

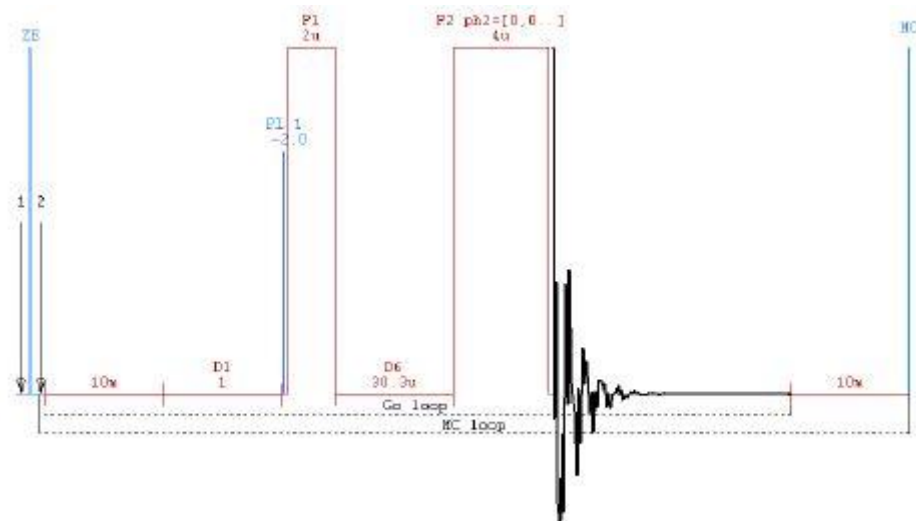


**Figure 3.6** The spin-echo (Hahn echo) pulse sequence of  $^7\text{Li}$  MAS NMR

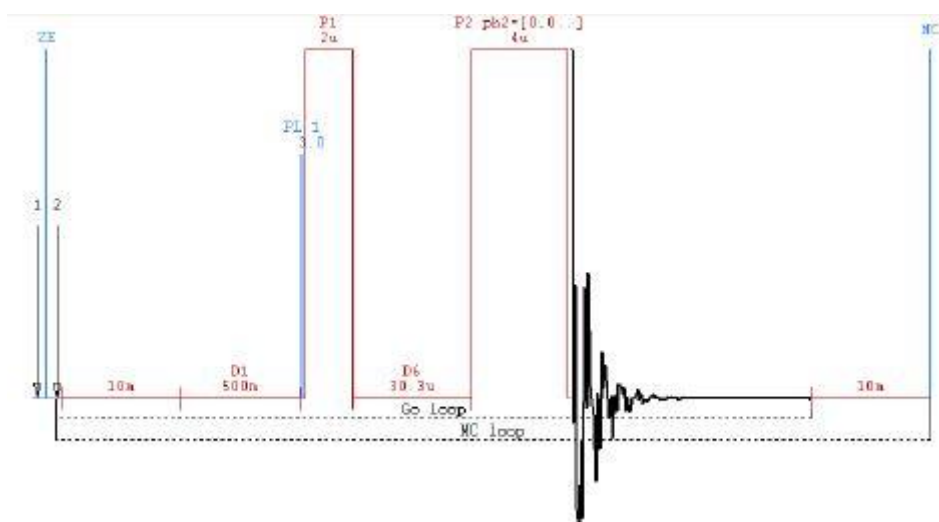


**Figure 3.7** The spin-echo (Hahn echo) pulse sequence of  $^{31}\text{P}$  MAS NMR

## **4. Results and Discussion**

### **4.1 General characterization of cathode materials**

#### **4.1.1 Thermo gravimetric (TG) and Differential Scanning Calorimetry (DSC)**

To determine the optimum sintering temperature and the solid-state reactions of the precursor mixture during the synthesis process, TG/DSC analyses were carried out for the precursor mixture before heat treatment as presented in Figure 4.1. The TG curve obviously shows that the present four evident steps of weight loss and DSC curve displays corresponding exothermic/endothemic peaks. The initial weight loss below 150 °C is due to the loss of physically adsorbed water. The main weight loss between 150 °C and 350 °C is ascribed to the loss of crystal water and the decomposition of reactants including the decomposition of ammonium, oxalate, and carbonate into NO<sub>2</sub>, CO<sub>2</sub>, CO, and H<sub>2</sub>O. The final small weight loss from 350 °C to 500 °C may correspond to the crystallization of the pyrophosphate. Above 500 °C, there is nearly no weight loss on TG curve, which indicates the complete crystallization of Li<sub>2</sub>FeP<sub>2</sub>O<sub>7</sub>. Therefore, it is suitable for sintering the precursor above 500 °C to gain Li<sub>2</sub>FeP<sub>2</sub>O<sub>7</sub>. However, endothermic peak appears in DSC curve at 710 °C and when the temperature reaches over 700 °C, the LiFePO<sub>4</sub> and Fe<sub>2</sub>P impurities will emerge in the composites. Using the TG/DSC curve as a guide, we sintered the precursor in the 500-700 °C temperature range.

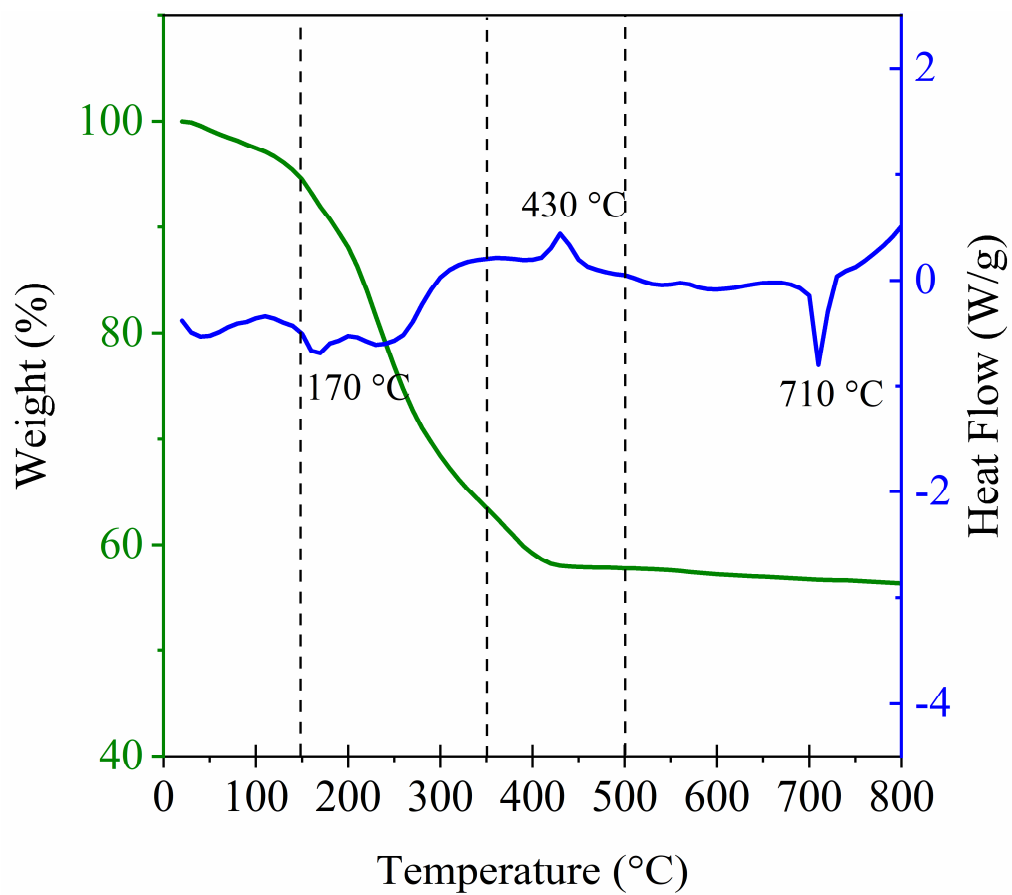


**Figure 4.1** TG/DSC curve of the precursor under flowing nitrogen.

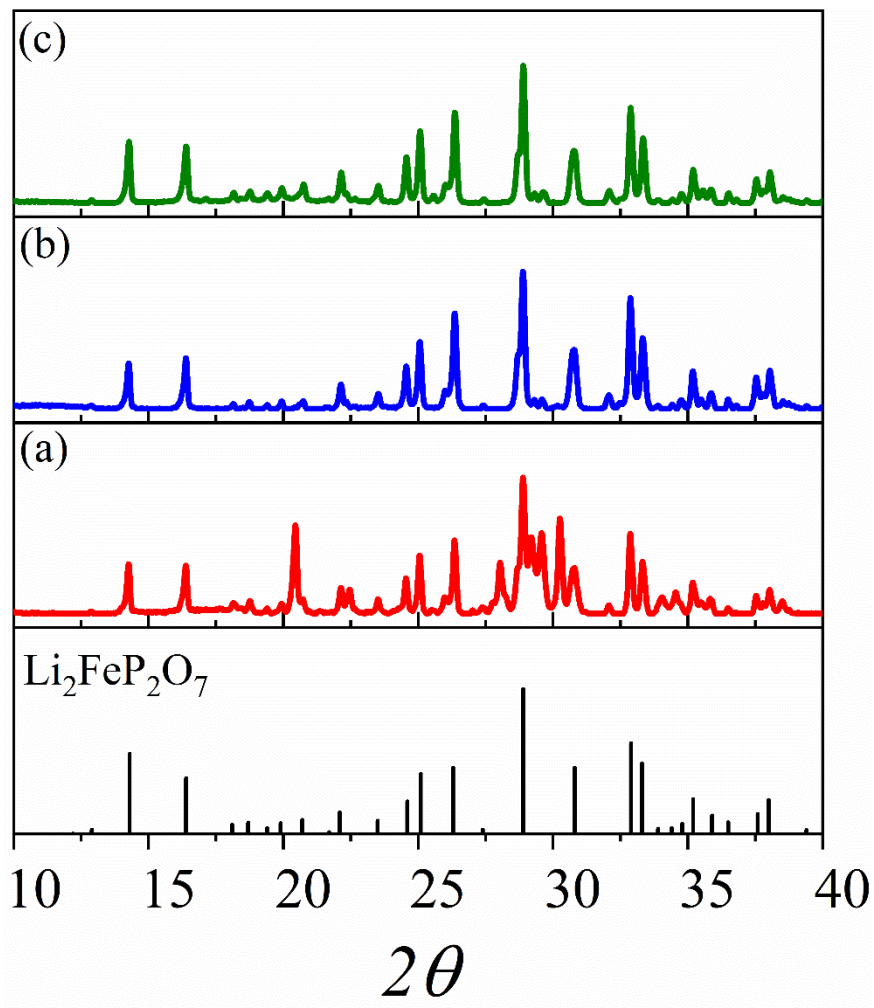
#### 4.1.2 X-ray Diffraction (XRD) for structural characterization

XRD is useful for determining the crystal structure of a solid sample by measuring the diffraction according to the angle change of the X-ray irradiating the sample.  $\text{Li}_2\text{FeP}_2\text{O}_7$  material has been measured at different sintering temperatures of 500 °C, 600 °C, and 650 °C, respectively. XRD patterns in Figure 4.2 is a comparative XRD pattern shows the effect of annealing temperature on the phase evolution of  $\text{Li}_2\text{FeP}_2\text{O}_7$ . High-temperature treatment slowly transforms this complex to form the final product. Single-phase product was obtained at 600 °C onwards. Therefore, the sintering temperature was selected to 600 °C

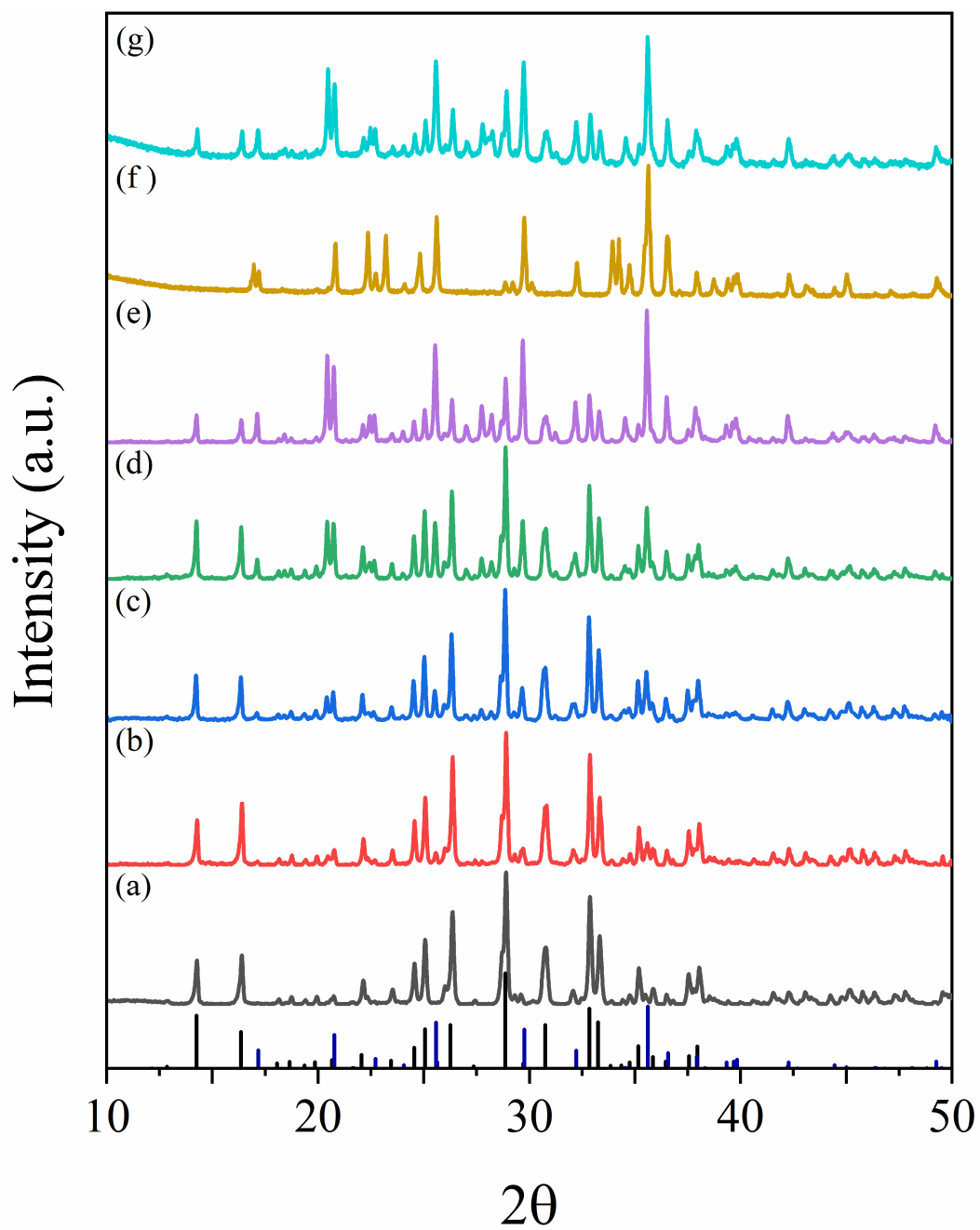
The XRD pattern of  $\text{Li}_2\text{FeP}_2\text{O}_{7-x}\text{F}_{2x}$  ( $x = 0, 0.01, 0.03, 0.05, 0.10, 0.50$  and  $1.00$ ) compound synthesized at 600 °C based on the TG/DSC analysis results is shown in Figure 4.3. As shown in Figure 4.3(a), all the peaks are sharp and no reflections are detected, indicating that the compounds are well crystallized, which are in accordance with the literature values. The observed XRD profile clearly indicates the formation of a single phase at pristine of monoclinic  $\text{Li}_2\text{FeP}_2\text{O}_7$  phase (JCPDS PDF No.: 78-2294, space group  $\text{P}2_1/\text{c}$ )<sup>66</sup> as reported previously. Also, the Rietveld refinement profiles of  $\text{Li}_2\text{FeP}_2\text{O}_{7-x}\text{F}_{2x}$  ( $x = 0$  and  $1.00$ ) are provided in Figure 4.4 and Table 4.1 for further observation of its fine structure. The red dot is experimental data points, black line is calculated powder pattern, green tick is Bragg positions of  $\text{Li}_2\text{FeP}_2\text{O}_7$ , and the blue line represents the difference between observed and calculated patterns.

Figure 4.3(b) ~ (g) show a pattern of  $\text{Li}_2\text{FeP}_2\text{O}_{7-x}\text{F}_{2x}$  ( $x = 0.01, 0.03, 0.05, 0.10, 0.50$  and  $1.00$ ) substituted with fluorine, respectively. We could observe the change of phase when compared with the pristine sample. It presents a mixed phase of the formation of  $\text{Li}_2\text{FeP}_2\text{O}_7$  and  $\text{LiFePO}_4$ .





**Figure 4.2** The XRD pattern of  $\text{Li}_2\text{FeP}_2\text{O}_7$  sintered at each temperature. (a) 500 °C, (b) 600 °C and (c) 650 °C.



**Figure 4.3** XRD patterns of  $\text{Li}_2\text{FeP}_2\text{O}_{7-x}\text{F}_{2x}$  for  $x =$  (a) 0, (b) 0.01, (c) 0.03, (d) 0.05, (e) 0.10, (f) 0.50 and (g) 1.00. Black lines represent lithium iron pyrophosphate reference and Blue lines are represented lithium iron phosphate.

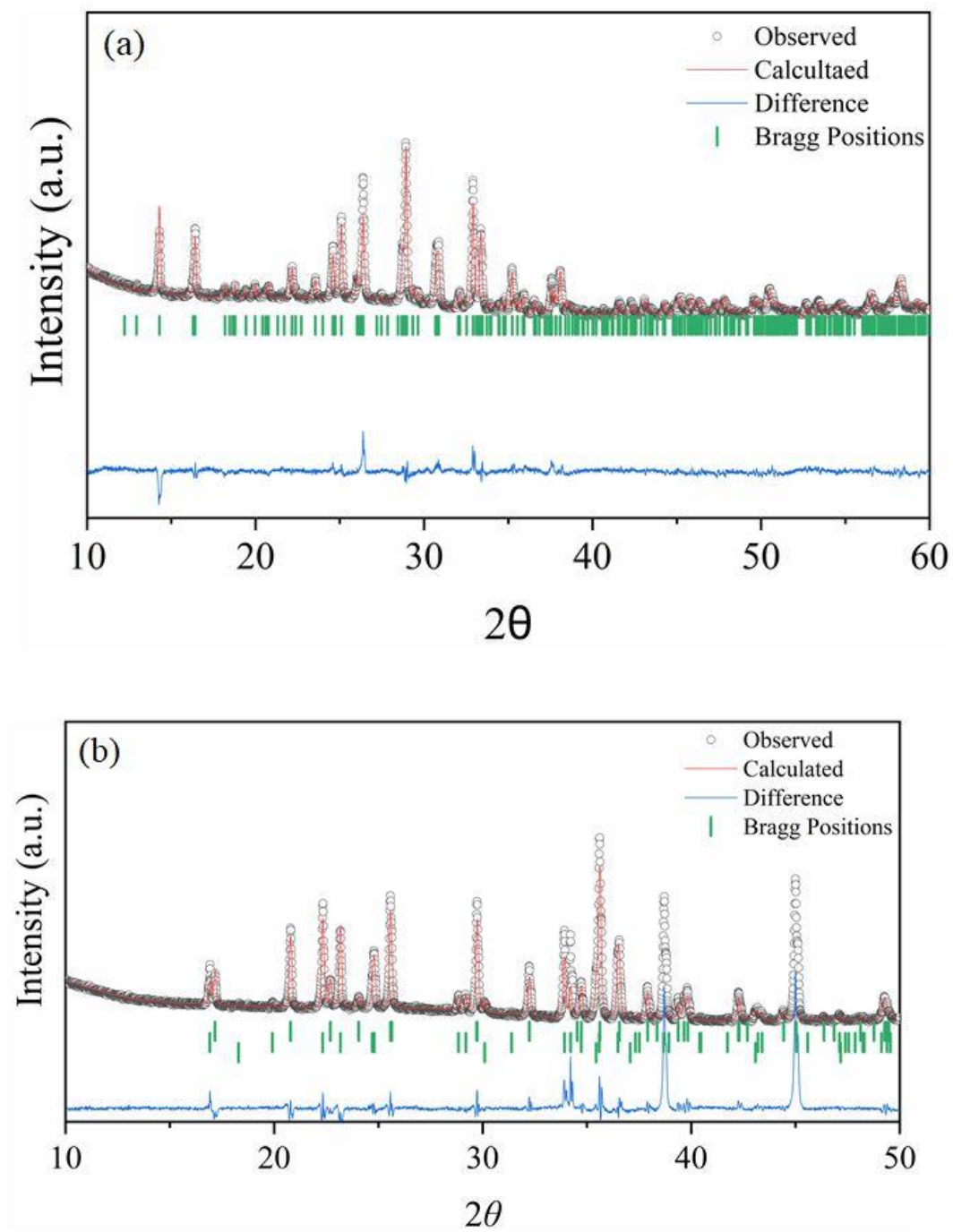


Figure 4.4 Rietveld refinements of the XRD patterns of  $\text{Li}_2\text{FeP}_2\text{O}_{7-x}\text{F}_{2x}$   $x=$  (a) 0 and (b) 1.00.

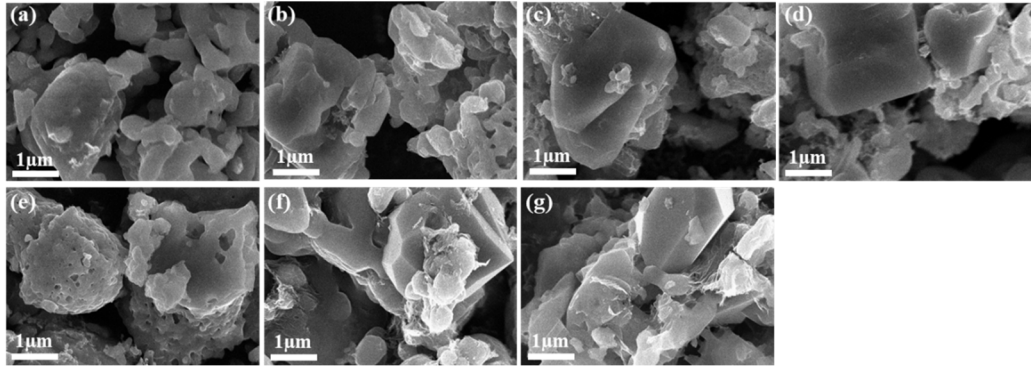
**Table 4.1** Lattice parameters of  $\text{Li}_2\text{FeP}_2\text{O}_7-x\text{F}_{2x}$  ( $x = 0$  and  $0.10$ )

	a (Å)	b (Å)	c (Å)	$\alpha$	$\beta$	$\Gamma$
x = 0	11.014	9.75065	9.80147	90.0°	101.5°	90.0°
x = 0.10	10.3226	6.00299	4.68861	90.0°	90.0°	90.0°

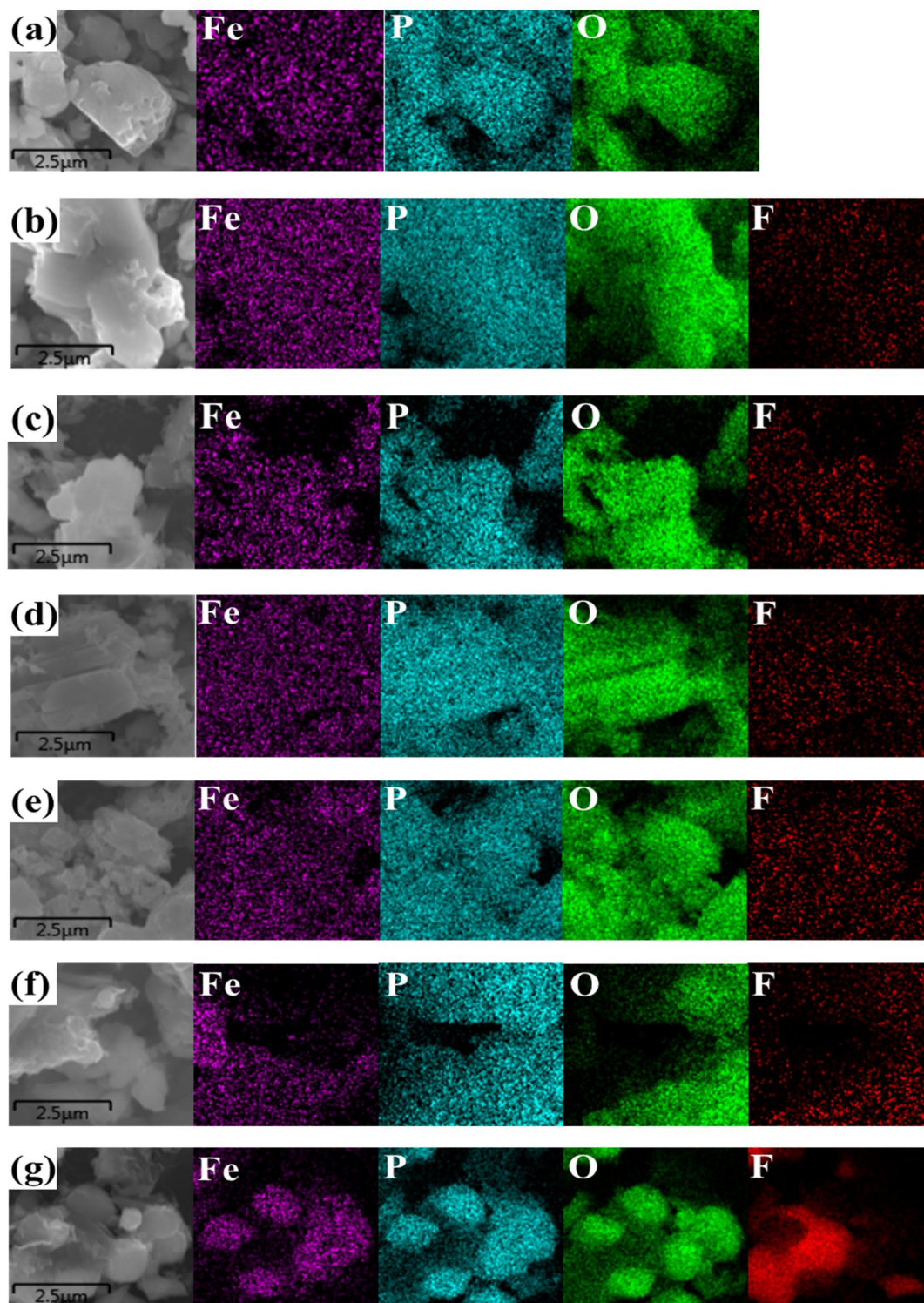
### **4.1.3 Scanning Electron Microscopy (FE-SEM) and Transmission electron Microscopy (TEM) analysis for particle size and morphology**

The morphologies of the as prepared samples were examined by FE-SEM. The FE-SEM images of  $\text{Li}_2\text{FeP}_2\text{O}_{7-x}\text{F}_{2x}$  series ( $x=0, 0.01, 0.03, 0.05, 0.10, 0.50,$  and  $1.00$ ) are shown in Figure 4.5. It can be seen that the average particle size of all samples is in the micrometer range. Also, the particle's shape is agglomerated to form larger clusters, showing similarly irregular shapes. Aggregation occurs as the gasification proceeds during the sintering process after milling. In addition, the edge can be identified as a feature of the solid-state method. There were no obvious changes in morphologies observed after doping with  $\text{F}^-$ . In addition, EDS dot mapping of Fe, P, O, and F in  $\text{Li}_2\text{FeP}_2\text{O}_{7-x}\text{F}_{2x}$  series were conducted in order to confirm the presence of doped elements. The doped elements were found to be uniformly distributed throughout the samples, as shown in Figure 4.6.

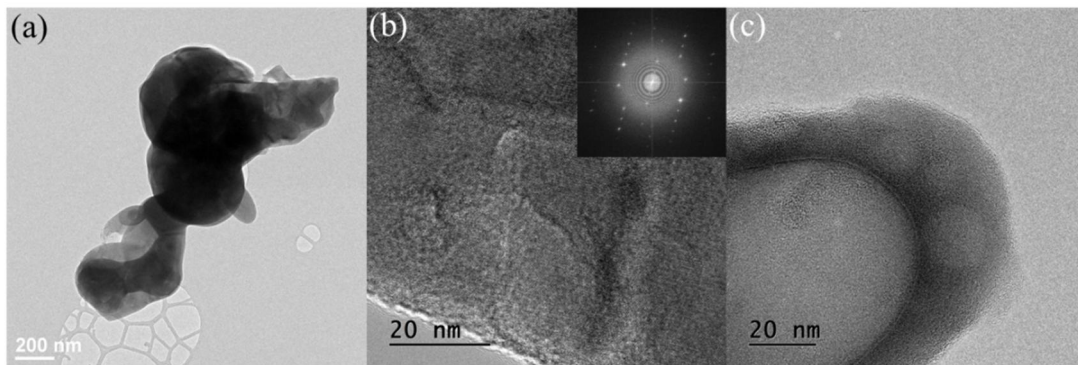
Bio-TEM was performed to determine the morphology of the particle by using cryo-holder. And, HR-TEM was performed to determine the lattice and morphology of the particles. TEM images of  $\text{Li}_2\text{FeP}_2\text{O}_7$  and  $\text{Li}_2\text{FeP}_2\text{O}_{6.90}\text{F}_{0.20}$  particles are shown in Figure 4.7. The HR-TEM image of a  $\text{Li}_2\text{FeP}_2\text{O}_7$  indicates that the particle is both structurally uniform and highly crystalline, while the lattice spacing of 0.32 nm is consistent with that of the (4 2 0) plane. Figure 4.7(c) shows that fluorine doping causes the change in physical properties.



**Figure 4.5** SEM images of the  $\text{Li}_2\text{FeP}_2\text{O}_{7-x}\text{F}_{2x}$   $x =$  (a) 0, (b) 0.01, (c) 0.03, (d) 0.05, (e) 0.10, (f) 0.50 and (g) 1.00.



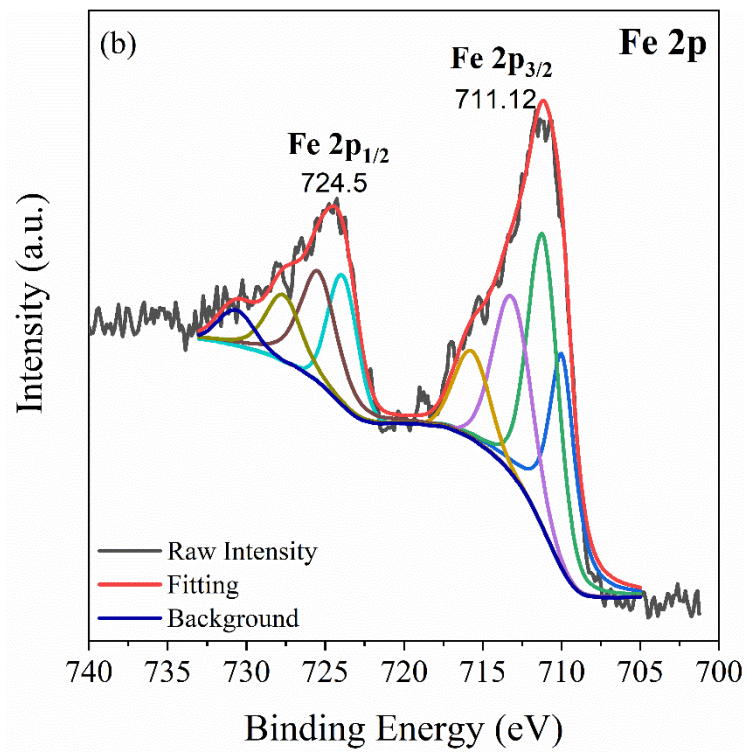
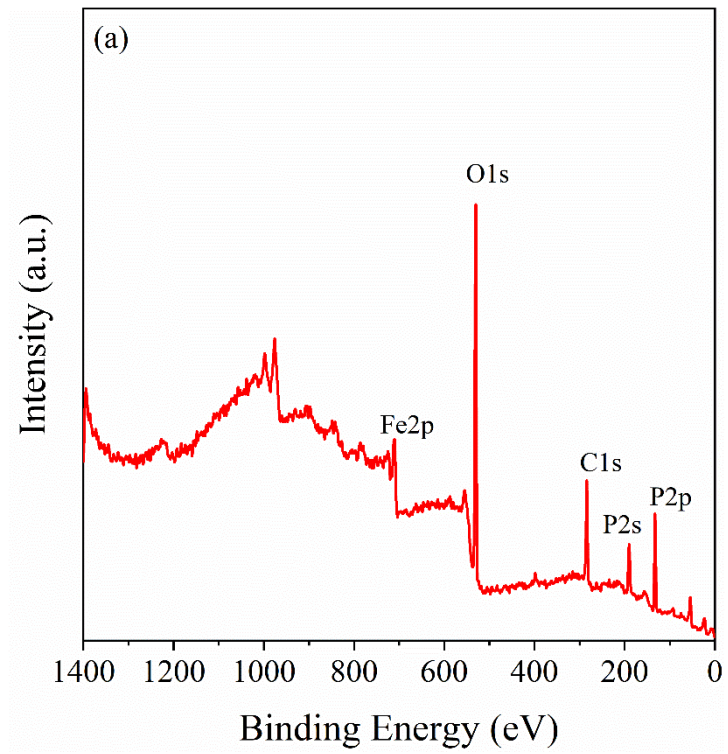
**Figure 4.6** EDX elemental mapping of the  $\text{Li}_2\text{FeP}_2\text{O}_{7-x}\text{F}_{2x}$   $x =$  (a) 0, (b) 0.01, (c) 0.03, (d) 0.05, (e) 0.10, (f) 0.50, and (g) 1.00.



**Figure 4.7** (a) Bio-TEM images of  $\text{Li}_2\text{FeP}_2\text{O}_7$ , HR-TEM images of  $\text{Li}_2\text{FeP}_2\text{O}_{7-x}\text{F}_{2x}$  (b)  $x = 0$  (c)  $x = 0.10$ . (Inset) SEAD patterns images of pristine

#### 4.14 X-ray photoelectron spectroscopy (XPS)

XPS is a surface-sensitive quantitative spectroscopic technique that normally measures the elemental composition with a monochromatic X-ray under ultra-high vacuum. Figure 4.8(b) and (c) show the Fe2p XPS spectra of the pristine  $\text{Li}_2\text{FeP}_2\text{O}_7$  and F doped  $\text{LiFeP}_2\text{O}_{6.9}\text{F}_{0.2}$ . As shown in Figure 4.8, the XPS spectra of Fe2p within samples all have two peaks. The major peak is observed at around 711 eV and the satellite peak at 725 eV. These peaks are assigned to  $\text{Fe}2p_{3/2}$  and  $\text{Fe}2p_{1/2}$ , respectively, indicating the oxidation state of Fe is +2, which is in accordance with literature values.<sup>67, 68</sup> As can be seen from the corresponding F1s spectra in Figure 4.8(d), peaks were weakly observed at 685.13 eV in  $\text{Li}_2\text{FeP}_2\text{O}_{6.9}\text{F}_{0.2}$  sample. No peaks can be observed in the F1s spectrum of pristine  $\text{Li}_2\text{FeP}_2\text{O}_7$ , which is in agreement with the matrix-doping of F into  $\text{Li}_2\text{FeP}_2\text{O}_7$  lattice.



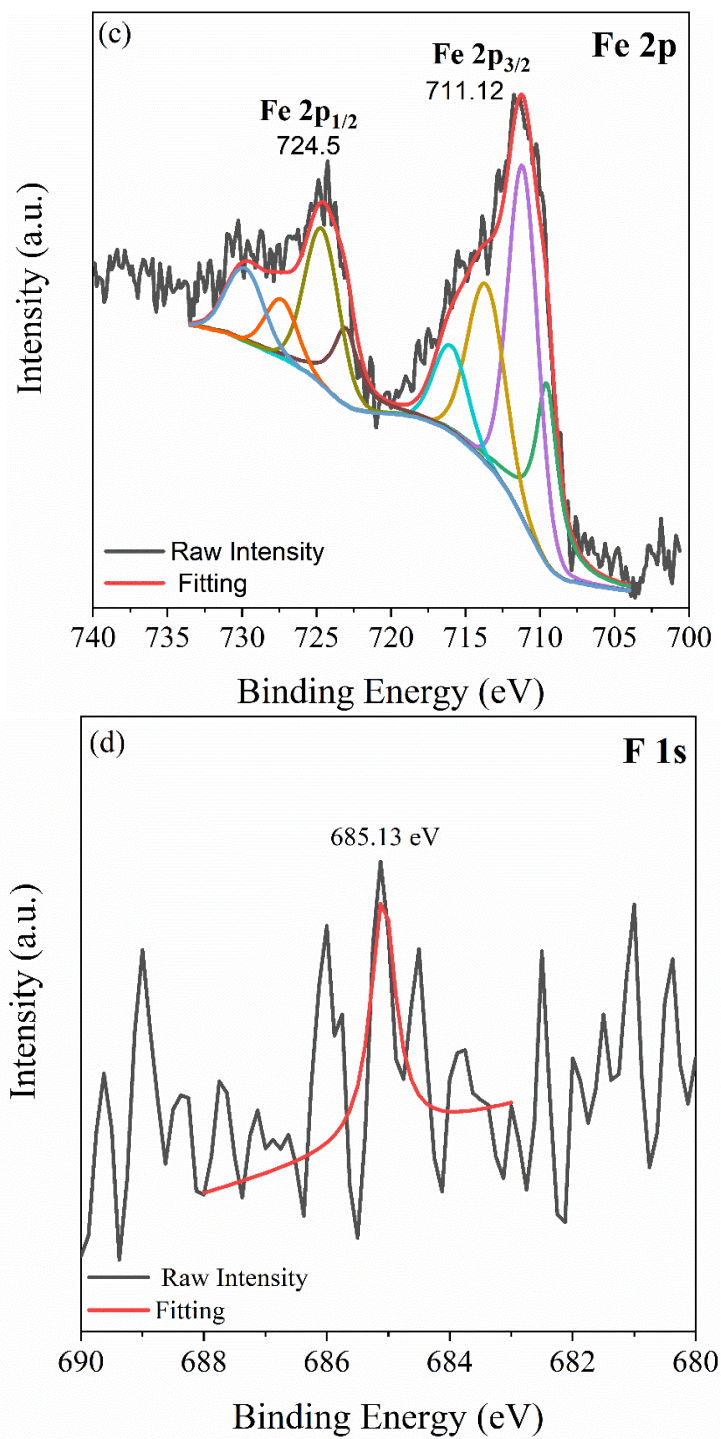


**Figure 4.8** XPS spectra of  $\text{Li}_2\text{FeP}_2\text{O}_7$  (a) survey, (b) Fe(2p), and spectra of  $\text{Li}_2\text{FeP}_2\text{O}_{6.9}\text{F}_{0.2}$  (c) Fe(2p), (d) F(1s).

## 4.2 Electrochemical study of synthesized cathode materials

### 4.2.1 Charge-discharge properties, Rate performance and long cycle abilities

The initial charge-discharge profiles of the  $\text{Li}_2\text{FeP}_2\text{O}_{7-x}\text{F}_{2x}$  ( $x = 0, 0.01, 0.03$  and  $0.05$ ) at  $0.05$  C rate are illustrated in Figure 4.9. Due to the potential decomposition of electrolyte caused by high emersion voltage of the second lithium ion, the range of test voltage was set as  $2.0$ - $4.3$  V. The 1<sup>st</sup> discharge capacity is  $73.17$ ,  $76.27$ ,  $73.38$ , and  $80.19$   $\text{mAh g}^{-1}$  for  $\text{Li}_2\text{FeP}_2\text{O}_{7-x}\text{F}_{2x}$  ( $x = 0, 0.01, 0.03$  and  $0.05$ ), respectively. Their specific capacity did not differ significantly. Instead, the fluorine substituted sample exhibits with plateaus at around  $3.4$  V. When the cycling evolves, there is a move of the plateaus to lower capacities and a small modification on the voltage of the plateaus potential. It can be seen that fluorine substitution has great effect on the electrochemical performance of the composite. Besides, the charge and discharge voltage plateaus reflect the two-phase nature of the lithium extraction and insertion reactions between  $\text{Li}_2\text{FeP}_2\text{O}_7$  and  $\text{LiFeP}_2\text{O}_7$ .

The rate performance of  $\text{Li}_2\text{FeP}_2\text{O}_{7-x}\text{F}_{2x}$  ( $x=0, 0.01, 0.03$ , and  $0.05$ ) are shown in Figure 4.10. The cells were cycled at  $0.05, 0.1, 0.2, 0.5, 1.0$ , and  $2.0$  C in the voltage range of  $2.0 - 4.3$  V. The discharge capacities of all the samples decreased with increasing current density. As can be seen from the graph, the more fluorine is contained, the more charge and discharge in high C-rate are favorable.

The cycling performance of  $\text{Li}_2\text{FeP}_2\text{O}_{7-x}\text{F}_{2x}$  ( $x=0, 0.01, 0.03$ , and  $0.05$ ) at  $1\text{C}$  are shown in Figure 4.11. The capacity retention rates of the materials after the 100<sup>th</sup> cycles were  $98, 99, 99$  and  $91$  %, respectively. The outstanding cycling performance of  $\text{Li}_2\text{FeP}_2\text{O}_{7-x}\text{F}_{2x}$  series was confirmed.

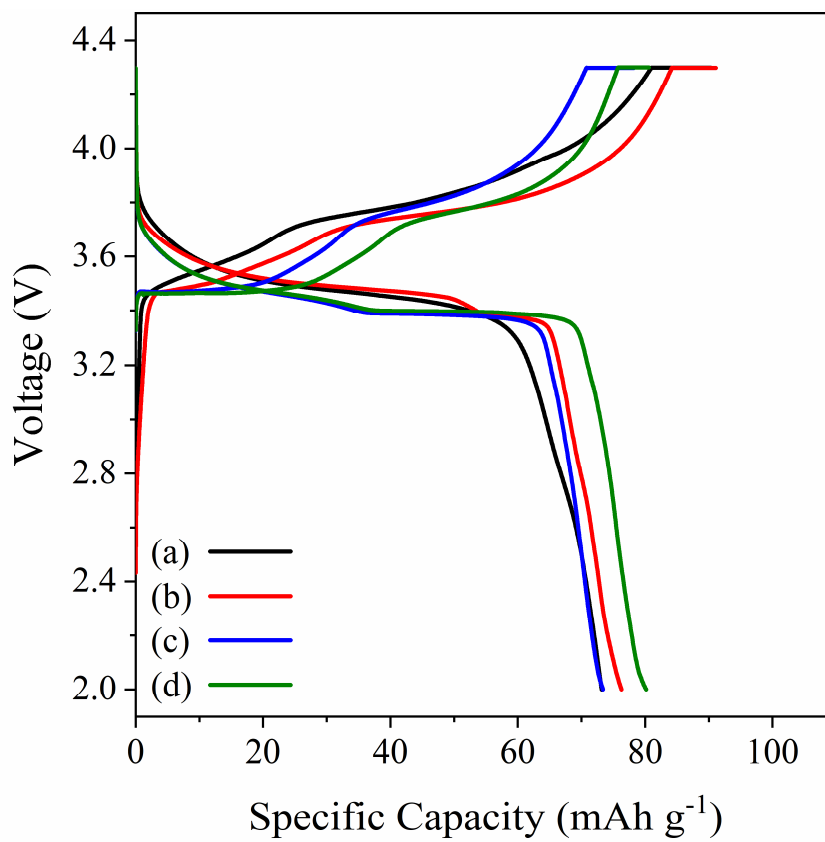


**Figure 4.9** 1<sup>st</sup> charge-discharge profile of  $\text{Li}_2\text{FeP}_2\text{O}_{7-x}\text{F}_{2x}$  series  $x =$  (a) 0, (b) 0.01, (c) 0.03, and (d) 0.05.

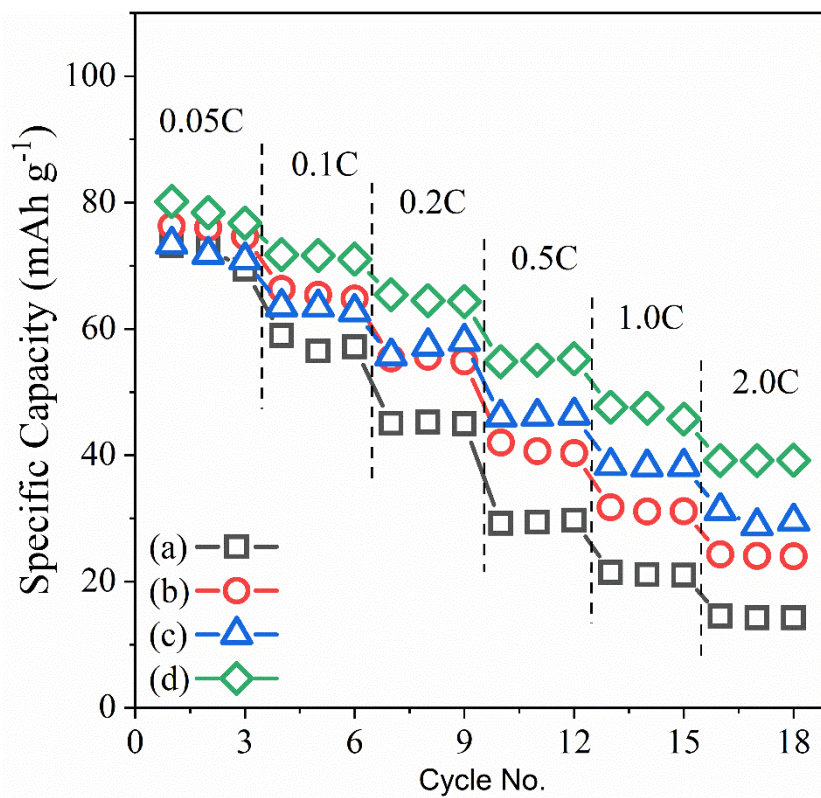


**Figure 4.10** The rate performance at various C-rate of  $\text{Li}_2\text{FeP}_2\text{O}_{7-x}\text{F}_{2x}$  series  $x =$  (a) 0, (b) 0.01, (c) 0.03, and (d) 0.05.

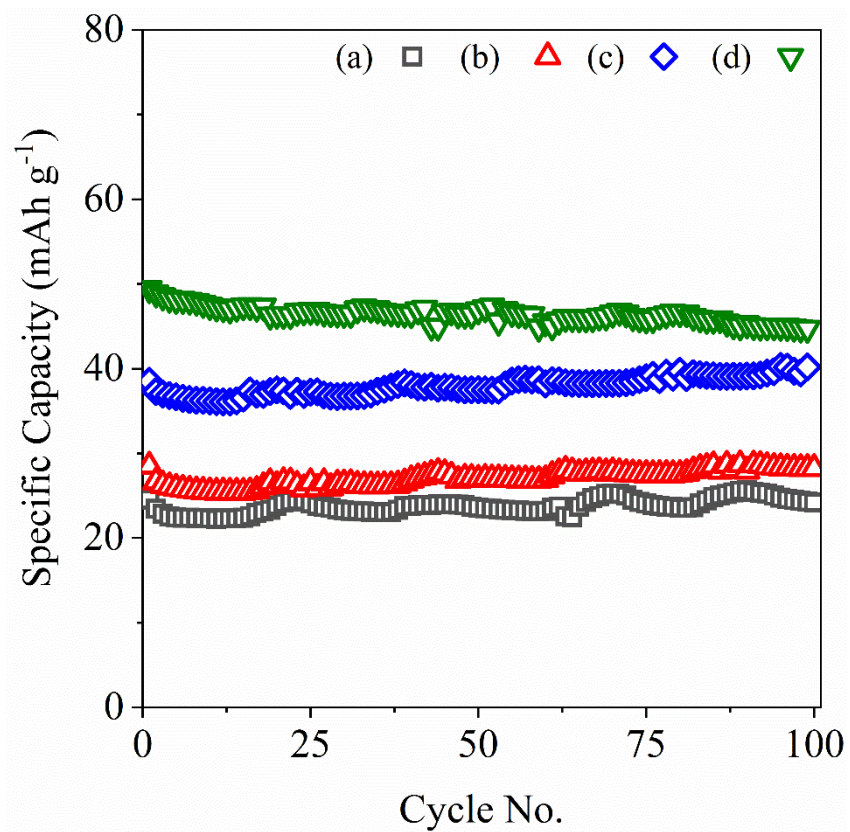


**Figure 4.11** The long cycle ability at 1C of  $\text{Li}_2\text{FeP}_2\text{O}_{7-x}\text{F}_{2x}$  series  $x =$  (a) 0, (b) 0.01, (c) 0.03, and (d) 0.05.

### 4.2.3 Cyclic voltammetry (CV)

Cyclic voltammetry (CV) is a widely used technique in electrochemistry that allow measuring the current flow by controlling the potential of the working electrode. The CV is a powerful tool to study the electrochemical behavior of a system by systematic study of current-voltage measurements of a given electrochemical cell.<sup>69</sup> The voltammogram gives us information about the redox reactions of the system, including the Faradaic reaction, surface reaction, and their reversibility.

Figure 4.12 shows three cycles of CV for  $\text{Li}_2\text{FeP}_2\text{O}_7$  synthesized at 650 . It can be seen that lithium sites are divided. It was observed that compound was not synthesized as a single phase. Considering TG/DSC and XRD results mentioned earlier, the appropriate synthesis temperature was determined to be 600 .

Cyclic voltammetry testing of  $\text{Li}_2\text{FeP}_2\text{O}_{7-x}\text{F}_{2x}$  ( $x = 0, 0.01, 0.03$  and  $0.05$ ) was conducted within the range of 2.0-4.3 V at a scan rate of  $0.05 \text{ mV s}^{-1}$ , as shown in Figure 4.13. The potential interval between the oxidation peak and reduction peak is an important parameter to evaluate the electrochemical performance. It can be observed that there are two anodic peaks and one cathodic peak. During the cathodic scan, an intensity peak (reduction peak) is obtained at 3.4 V, corresponding to the insertion of lithium ions into the bulk material. During the anodic scan, the oxidation peak consists of two peaks at approximately 3.6 V and 3.8 V, corresponding to the  $\text{Fe}^{2+}/\text{Fe}^{3+}$  redox couple.<sup>66</sup> These two voltage regions correspond to the preferential oxidation of different iron sites in  $\text{Li}_2\text{FeP}_2\text{O}_7$  due to the two different coordination numbers of  $\text{FeO}_5$  and  $\text{FeO}_6$  in crystal structure. It is important to note that relatively sharper peaks observed in  $\text{F}^-$  substituted samples point out the more stable insertion and extraction processes of lithium ions. Second lithium extraction corresponding

to  $\text{Fe}^{3+}/\text{Fe}^{4+}$  redox couple or the oxidation of electrolyte at high potential need further research.

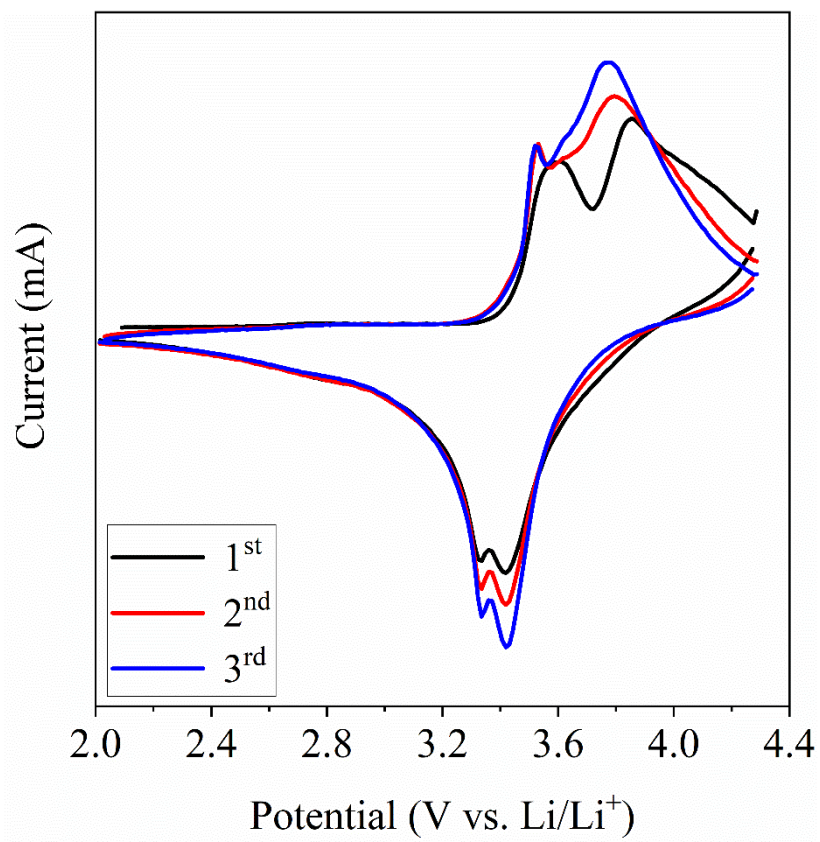


**Figure 4.12** Voltammogram of  $\text{Li}_2\text{FeP}_2\text{O}_7$  synthesized at 650

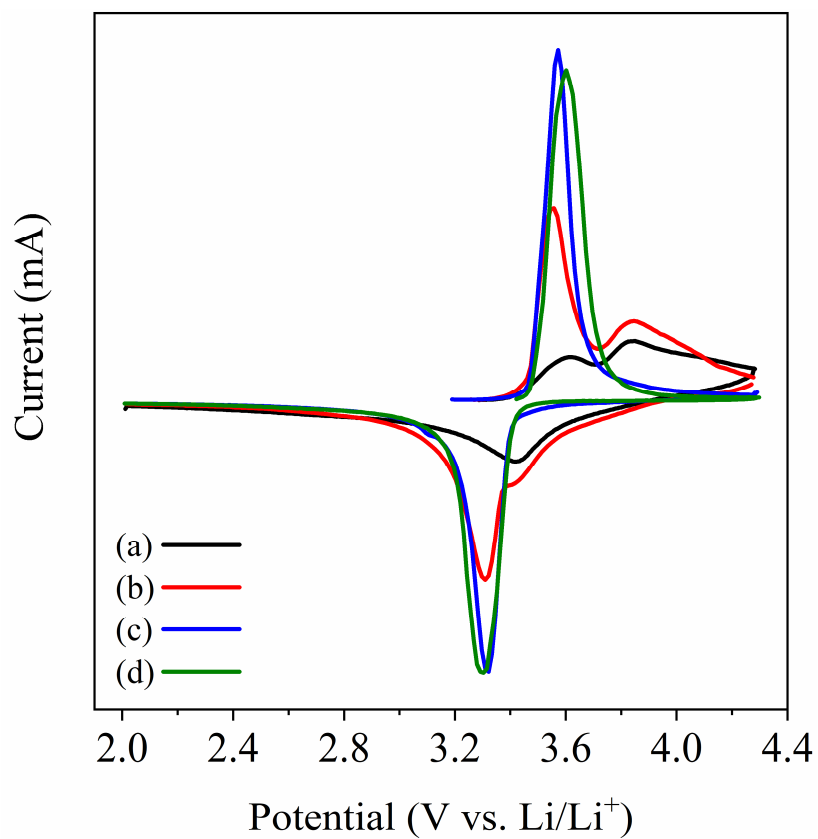


**Figure 4.13** Cyclic voltammetry (CV) of  $\text{Li}_2\text{FeP}_2\text{O}_7-x\text{F}_{2x}$   $x =$  (a) 0, (b) 0.01, (c) 0.03, and (d) 0.05.

### 4.3 MAS NMR for structural characterization

#### 4.3.1 $^7\text{Li}$ MAS NMR

The  $^7\text{Li}$  magic angle spinning (MAS) NMR studies of lithium iron pyrophosphate is carried out to investigate the local environment of lithium atoms.  $^7\text{Li}$  MAS NMR is a useful analytical method for investigating the local environment of lithium participating in electrochemical reactions in cathode materials.  $^7\text{Li}$  MAS NMR measurements were used to compare the chemical shift of  $\text{Li}_2\text{FeP}_2\text{O}_{7-x}\text{F}_{2x}$  ( $x = 0, 0.01, 0.03, 0.05$  and  $0.10$ ) according to the fluorine substitution ratio. As shown in Figure 4.14(a) and (b), a single isotropic peak for samples  $\text{Li}_2\text{FeP}_2\text{O}_{7-x}\text{F}_{2x}$  ( $x = 0$  and  $0.01$ ) appear at around 10 ppm pointed out by dashed line and spinning side bands marked by asterisks (\*) Increasing the fluorine substitution ratio results in shift of isotropic peak to around -20 ppm, as shown in Figure 4.14 (c) ~ (e). This peak shift of 0.5% of the total spectrum width is associated to fluorine doping effect. This change can be thought to be the result of substitution effect by fluorine anion, not structural change of lithium. Despite single isotropic peak, these results don't imply that these elements exist as a single site on their crystal structure. It has to be considered as the superimposition of signals coming from distribution of several lithium ion sites.<sup>70</sup> Additionally, peak of fluorine substituted samples are more sharper compared to those of pristine.

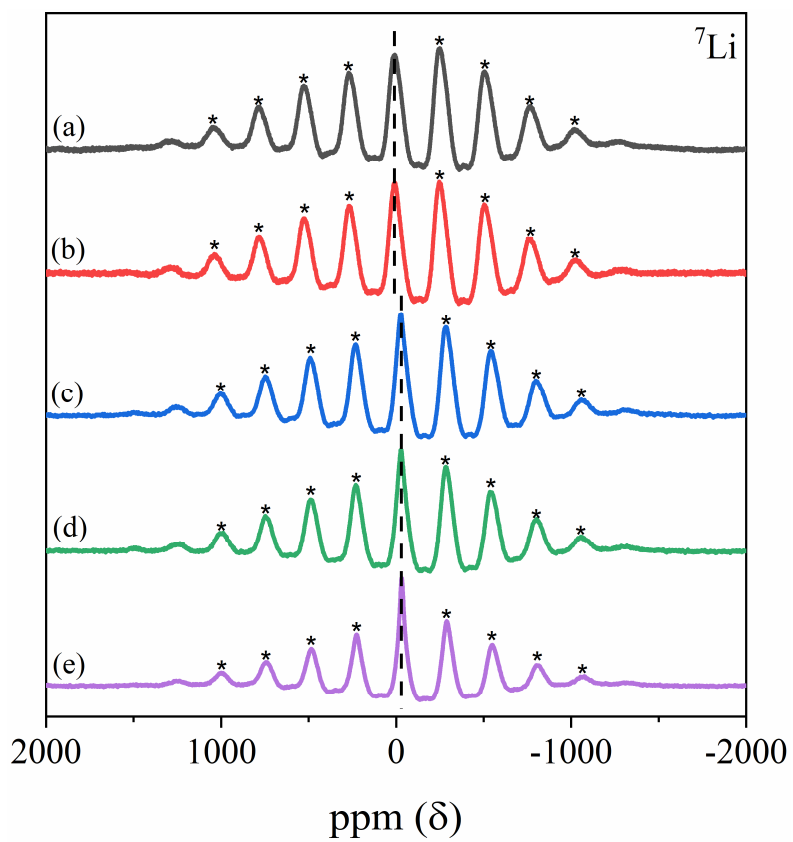


**Figure 4.14**  ${}^7\text{Li}$  MAS NMR spectra of the  $\text{Li}_2\text{FeP}_2\text{O}_{7-x}\text{F}_{2x}$  series  $x =$  (a) 0, (b) 0.01, (c) 0.03, (d) 0.05, and (e) 0.10 at 30 kHz. Isotropic peak is marked as dash line and the spinning sidebands are marked with asterisks (\*).

### 4.3.2 $^{31}\text{P}$ MAS NMR

Figure 4.15 illustrates the  $^{31}\text{P}$  MAS NMR about  $\text{Li}_2\text{FeP}_2\text{O}_7\text{-xF}_{2\text{x}}$  series.  $^{31}\text{P}$  MAS NMR is a useful analytical method for investigating the local environment of lithium participating in electrochemical reactions in cathode materials. In the  $\text{PO}_4$  unit has strong covalent bonds<sup>19</sup> and has almost tetrahedral geometry, precluding any significant CSA interaction for the  $^{31}\text{P}$  nucleus. On the basis of this information, we expect a single, featureless  $^{31}\text{P}$  resonance, possibly accompanied by a sideband manifold arising from paramagnetic coupling and bulk magnetic susceptibility.<sup>71</sup>

The  $^{31}\text{P}$  MAS NMR shows the existence of a single resonance peak around 4950 ppm pointed out by dash line and spinning side bands are marked by asterisks (\*) corresponding to the lithium site in  $\text{Li}_2\text{FeP}_2\text{O}_7$ . Also, Fluorine substituted samples show that the existence of a single isotropic peak around 4000 ppm. Although fluorine substituted samples have negligible peak shift, there isn't much meaning because their differences are solely 0.8 % of the total spectrum width.

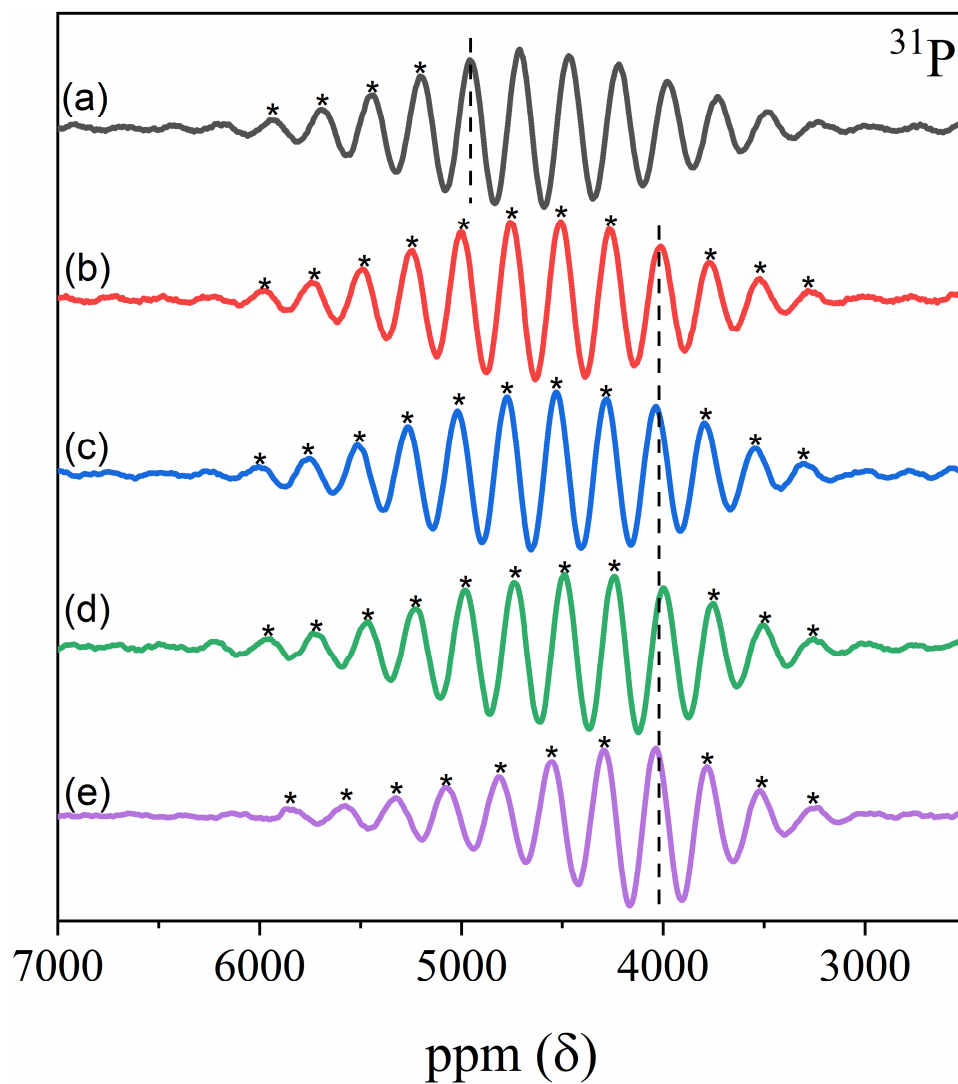


**Figure 4.15**  $^{31}\text{P}$  MAS NMR spectra of the  $\text{Li}_2\text{FeP}_2\text{O}_{7-x}\text{F}_{2x}$  series  $x =$  (a) 0, (b) 0.01, (c) 0.03, (d) 0.05, and (e) 0.10 at 30 kHz. Isotropic peak is marked as dash line and the spinning sidebands are marked with asterisks (\*).

## 5. Conclusions

The preparation of  $\text{Li}_2\text{FeP}_2\text{O}_7$  cathode material for lithium-ion batteries was carried out by the solid-state method considering various requirements. In addition, wide investigation including structural, surface properties and electrochemical characteristics was performed for considering effects of preparation methods on cathode materials. Thermal analysis of the precursor was performed and synthesized from 500 to 700 °C for optimizing sintering temperature. The XRD results reveal that the same crystal structures were obtained when calcination temperature was 600 and 650 °C. But, according to CV measurement, single crystal grains are formed at 600 °C. Therefore, fluorine anion doping was performed at 600 °C. SEM and TEM images were used to confirm the morphology and chemical or physical property change. The presence and oxidation state of Fe and F element was confirmed through XPS. Solid-state NMR was measured in order to perform structural analysis through  $^7\text{Li}$  and  $^{31}\text{P}$  nucleus. The single isotropic peak and spinning sideband were confirmed by MAS method. In structural characterization analysis, we have confirmed that Fluorine anion doping at oxygen site enables structural modification from  $\text{P}_2\text{O}_7$  to  $\text{PO}_4$ . The fluorinated samples show greater overall electrochemical performance. In particular, Fluorine doping of lithium iron pyrophosphate has enhanced electronic conductivity and showed higher specific capacity at high C-rate. Moreover, there are no pronounced changes occurs in the shape and peak intensity for the subsequent cycles, indicating that these materials have good cycling stability and reversibility.

## 6. Reference

1. Kordesch, K., ELECTROCHEMICAL ENERGY STORAGE. In *Energy Storage*, Silverman, J., Ed. Pergamon: 1980; pp 8-34.
2. Sugumaran, N.; Everill, P.; Swogger, S. W.; Dubey, D. P., Lead acid battery performance and cycle life increased through addition of discrete carbon nanotubes to both electrodes. *Journal of Power Sources* **2015**, *279*, 281-293.
3. Altavilla, C.; Claudia; Ciliberto, E.; Ciliberto, E., *Inorganic Nanoparticles: Synthesis, Applications, And Perspectives*. 2011.
4. Ozawa, K., Lithium-ion rechargeable batteries with LiCoO<sub>2</sub> and carbon electrodes: the LiCoO<sub>2</sub>/C system. *Solid State Ionics* **1994**, *69* (3), 212-221.
5. EPEC, Battery Comparison of Energy Density. **2017**.
6. Whittingham, M. S., Lithium Batteries and Cathode Materials. *Chemical Reviews* **2004**, *104* (10), 4271-4302.
7. Roy, P.; Srivastava, S. K., Nanostructured anode materials for lithium ion batteries. *Journal of Materials Chemistry A* **2015**, *3* (6), 2454-2484.
8. Chen, J.; Cheng, F., Combination of Lightweight Elements and Nanostructured Materials for Batteries. *Accounts of Chemical Research* **2009**, *42* (6), 713-723.
9. He, P.; Yu, H.; Li, D.; Zhou, H., Layered lithium transition metal oxide cathodes towards high energy lithium-ion batteries. *Journal of Materials Chemistry* **2012**, *22* (9), 3680-3695.
10. Armstrong, M. J.; O'Dwyer, C.; Macklin, W. J.; Holmes, J. D., Evaluating the performance of nanostructured materials as lithium-ion battery electrodes. *Nano Res.* **2014**, *7* (1), 1-62.
11. Amatucci, G. G.; Tarascon, J. M.; Klein, L. C., Cobalt dissolution in LiCoO<sub>2</sub>-

- based non-aqueous rechargeable batteries. *Solid State Ionics* **1996**, *83* (1), 167-173.
12. Amatucci, G. G.; Tarascon, J. M.; Klein, L. C., CoO<sub>2</sub>, the end member of the Li<sub>x</sub>CoO<sub>2</sub> solid solution. *J. Electrochem. Soc.* **1996**, *143* (3), 1114-23.
  13. Deng, B.; Nakamura, H.; Yoshio, M., Capacity fading with oxygen loss for manganese spinels upon cycling at elevated temperatures. *Journal of Power Sources* **2008**, *180* (2), 864-868.
  14. Li, G.; Azuma, H.; Tohda, M., LiMnPO<sub>4</sub> as the cathode for lithium batteries. *Electrochem. Solid-State Lett.* **2002**, *5* (6), A135-A137.
  15. Thackeray, M. M.; Johnson, P. J.; de Picciotto, L. A.; Bruce, P. G.; Goodenough, J. B., Electrochemical extraction of lithium from LiMn<sub>2</sub>O<sub>4</sub>. *Materials Research Bulletin* **1984**, *19* (2), 179-187.
  16. Niu, Y.; Zhang, Y.; Xu, M., A review on pyrophosphate framework cathode materials for sodium-ion batteries. *Journal of Materials Chemistry A* **2019**, *7* (25), 15006-15025.
  17. Fisher, C. A. J.; Hart Prieto, V. M.; Islam, M. S., Lithium Battery Materials LiMPO<sub>4</sub> (M = Mn, Fe, Co, and Ni): Insights into Defect Association, Transport Mechanisms, and Doping Behavior. *Chemistry of Materials* **2008**, *20* (18), 5907-5915.
  18. Nishimura, S.-i.; Nakamura, M.; Natsui, R.; Yamada, A., New Lithium Iron Pyrophosphate as 3.5 V Class Cathode Material for Lithium Ion Battery. *Journal of the American Chemical Society* **2010**, *132* (39), 13596-13597.
  19. Naoi, K.; Iwamizu, Y.; Mori, M.; Naruoka, Y., Enhancement of electrochemical performance of disulfide using polyvinylpyridine film. *J. Electrochem. Soc.* **1997**, *144* (4), 1185-1188.
  20. Padhi, A.; Nanjundaswamy, K. S.; Goodenough, J., Phospho-Olivines as Positive-

Electrode Materials for Rechargeable Lithium Batteries. *Journal of The Electrochemical Society* **1997**, *144*, 1188-1194.

21. Yuan, L.-X.; Wang, Z.-H.; Zhang, W.-X.; Hu, X.-L.; Chen, J.-T.; Huang, Y.-H.; Goodenough, J. B., Development and challenges of LiFePO<sub>4</sub> cathode material for lithium-ion batteries. *Energy & Environmental Science* **2011**, *4* (2), 269-284.

22. Wang, J.; Niu, Y.; Fu, Y.; Yang, Y.; Hojamberdiev, M., Urea and Ethylene Glycol-Assisted Solvothermal Synthesis of Spheroidal LiFePO<sub>4</sub>/C Nanoparticles as a Cathode Material for Lithium-ion Batteries. **2018**, *3* (19), 5471-5479.

23. Liu, Q.-B.; Liao, S.-J.; Song, H.-Y.; Liang, Z.-X., High-performance LiFePO<sub>4</sub>/C materials: Effect of carbon source on microstructure and performance. *Journal of Power Sources* **2012**, *211*, 52-58.

24. Huang, Y.-G.; Zheng, F.-H.; Zhang, X.-H.; Li, Q.-Y.; Wang, H.-Q., Effect of carbon coating on cycle performance of LiFePO<sub>4</sub>/C composite cathodes using Tween80 as carbon source. *Electrochimica Acta* **2014**, *130*, 740-747.

25. Yang, Z.; Qiao, Q.; Kang, X.; Yang, W., Facile synthesis of nanostructured LiFePO<sub>4</sub>/C cathode material for lithium-ion batteries. *Chinese Science Bulletin* **2012**, *57* (32), 4160-4163.

26. Wang, D.; Li, H.; Shi, S.; Huang, X.; Chen, L., Improving the rate performance of LiFePO<sub>4</sub> by Fe-site doping. *Electrochimica Acta* **2005**, *50* (14), 2955-2958.

27. Srinivasan, V.; Newman, J., Existence of Path-Dependence in the LiFePO<sub>4</sub> Electrode. *Electrochem. Solid-State Lett.* **2006**, *9* (3), A110-A114.

28. Uebou, Y.; Okada, S.; Egashira, M.; Yamaki, J.-I., Cathode properties of pyrophosphates for rechargeable lithium batteries. *Solid State Ionics* **2002**, *148* (3), 323-328.

29. J.Barker, R. K. B. G., P. Burns, and A. Bryan, LiVP<sub>2</sub>O<sub>7</sub>: A Viable Lithium-Ion

Cathode Material? *Electrochemical and Solid-state Letters* **2005**, *8* (9), A446-A448.

30. Wurm, C.; Morcrette, M.; Rouse, G.; Dupont, L.; Masquelier, C., Lithium Insertion/Extraction into/from LiMX<sub>2</sub>O<sub>7</sub> Compositions (M = Fe, V; X = P, As) Prepared via a Solution Method. *Chemistry of Materials* **2002**, *14* (6), 2701-2710.

31. John M. Clark, D. S. i. N., Prof. Atsuo Yamada, Prof. M. Saiful Islam, High Voltage Pyrophosphate Cathode: Insights into Local Structure and Lithium Diffusion Pathways. *Angew.Chem.Int.Ed* **2012**, *51*, 13149-13153.

32. Lee, S.; Park, S. S., Structure, Defect Chemistry, and Lithium Transport Pathway of Lithium Transition Metal Pyrophosphates (Li<sub>2</sub>MP<sub>2</sub>O<sub>7</sub>, M: Mn, Fe, and Co): Atomistic Simulation Study. *Chemistry of Materials* **2012**, *24* (18), 3550-3557.

33. Blidberg, A.; Häggström, L.; Ericsson, T.; Tengstedt, C.; Gustafsson, T.; Björefors, F., Structural and Electronic Changes in Li<sub>2</sub>FeP<sub>2</sub>O<sub>7</sub> during Electrochemical Cycling. *Chemistry of Materials* **2015**, *27* (11), 3801-3804.

34. Nitta, N.; Wu, F.; Lee, J. T.; Yushin, G., Li-ion battery materials: present and future. *Materials Today* **2015**, *18* (5), 252-264.

35. Sin, b. c., Study of anion substitution effect on olivine structured cathode materials for lithium ion battery. **2015**.

36. Lu, F.; Zhou, Y.; Liu, J.; Pan, Y., Enhancement of F-doping on the electrochemical behavior of carbon-coated LiFePO<sub>4</sub> nanoparticles prepared by hydrothermal route. *Electrochimica Acta* **2011**, *56* (24), 8833-8838.

37. Pan, F.; Wang, W.-l., Synthesis and characterization of core-shell F-doped LiFePO<sub>4</sub>/C composite for lithium-ion batteries. *Journal of Solid State Electrochemistry* **2012**, *16* (4), 1423-1427.

38. Sun, C. S.; Zhang, Y.; Zhang, X. J.; Zhou, Z., Structural and electrochemical

- properties of Cl-doped LiFePO<sub>4</sub>/C. *Journal of Power Sources* **2010**, *195* (11), 3680-3683.
39. Lee, S.-B.; Cho, S.-H.; Kim, H.-S.; Lee, Y.-S., Improved Cycle Performance of Sulfur-Doped LiFePO<sub>4</sub> Material at High Temperatures. **2009**, *30*.
40. Wu, C.; Wu, F.; Chen, L.; Huang, X., Fabrications and electrochemical properties of fluorine-modified spinel LiMn<sub>2</sub>O<sub>4</sub> for lithium ion batteries. *Solid State Ionics* **2002**, *152-153*, 327-334.
41. Whitfield, P.; Davidson, I., Microwave synthesis of Li<sub>1.025</sub>Mn<sub>1.975</sub>O<sub>4</sub> and Li<sub>1+x</sub>Mn<sub>2-x</sub>O<sub>4</sub>-yF<sub>y</sub> (x = 0.05, 0.15; y = 0.05, 0.1). *ChemInform* **2001**, *32*.
42. Yonezawa, S.; Yamasaki, M.; Takashima, M., Surface fluorination of the cathode active materials for lithium secondary battery. *Journal of Fluorine Chemistry* **2004**, *125* (11), 1657-1661.
43. Zhong, S.; Liu, L.; Liu, J.; Wang, J.; Yang, J., High-rate characteristic of F-substitution Li<sub>3</sub>V<sub>2</sub>(PO<sub>4</sub>)<sub>3</sub> cathode materials for Li-ion batteries. *Solid State Communications - SOLID STATE COMMUN* **2009**, *149*, 1679-1683.
44. Liao, X.-Z.; He, Y.-S.; Ma, Z.-F.; Zhang, X.-M.; Wang, L., Effects of fluorine-substitution on the electrochemical behavior of LiFePO<sub>4</sub>/C cathode materials. *Journal of Power Sources* **2007**, *174* (2), 720-725.
45. Kubo, K.; Arai, S.; Yamada, S.; Kanda, M., Synthesis and charge-discharge properties of Li<sub>1+x</sub>Ni<sub>1-x-y</sub>Co<sub>y</sub>O<sub>2-z</sub>F<sub>z</sub>. *Journal of Power Sources* **1999**, *81-82*, 599-603.
46. Naghash, A. R.; Lee, J. Y., Lithium nickel oxyfluoride (Li<sub>1-z</sub>Ni<sub>1+z</sub>FyO<sub>2-y</sub>) and lithium magnesium nickel oxide (Li<sub>1-z</sub>(MgxNi<sub>1-x</sub>)<sub>1+z</sub>O<sub>2</sub>) cathodes for lithium rechargeable batteries: II. Electrochemical investigations. *Electrochimica Acta* **2001**, *46* (15), 2293-2304.
47. Jugović, D.; Mitrić, M.; Milović, M.; Cvjetičanin, N.; Jokić, B.; Umičević,

- A.; Uskoković, D., The influence of fluorine doping on the structural and electrical properties of the LiFePO<sub>4</sub> powder. *Ceramics International* **2017**, *43* (3), 3224-3230.
48. Robinson, J. W., Undergraduate Instrumental Analysis *CRC Process* **2005**.
49. [http://hiq.linde-gas.com/en/analytical\\_methods/nuclear\\_magnetic\\_resonance.html](http://hiq.linde-gas.com/en/analytical_methods/nuclear_magnetic_resonance.html).
50. Maciejewski, M., Basics of NMR Spectroscopy. **2016**.
51. Oliver Pecher, J. C.-G., Kent J. Griffith, and Clare P. Grey, Materials' Methods: NMR in Battery Research. *Chemistry of Materials* **2016**, *29*, 213-242.
52. <http://mriquestions.com/predict-nuclear-spin-i.html>.
53. Wu, S., 1D and 2D NMR Experiment Methods. **2011**.
54. Hirayama, Y.; Yusa, G.; Hashimoto, K.; Kumada, N.; Ota, T.; Muraki, K., Electron-spin/nuclear-spin interactions and NMR in semiconductors. *Semiconductor Science and Technology* **2009**, *24* (2), 023001.
55. Edward, J. C., Principle of NMR. **2009**, 87A.
56. Ridgway, J. P., Cardiovascular magnetic resonance physics for clinicians: part I. *Journal of Cardiovascular Magnetic Resonance* **2010**, *12* (1), 71.
57. Schurko, R., Introduction to Solid State NMR. **2002**, 1-30.
58. A. Alia, S. G., Huub J. M. de Groot, Magic angle spinning(MAS) NMR: a new tool to study the spatial and electronic structure of photosynthetic complexes. *Photosynthesis reserch* **2009**, *102* (2), 415-425.
59. Polenova, T., Spinning into focus. *Nature Chemistry* **2011**, 3.
60. Laboratory, N. H. M. F., Magic Angle Spinning Probe *Nationalmaglab* **2014**.
61. Matsuoka, S.; Inoue, M., Application of REDOR NMR in natural product chemistry. *Chem. Commun. (Cambridge, U. K.)* **2009**, (38), 5664-5675.
62. Taulelle, F., Fundamental Principles of NMR Crystallography. **2009**, 245-262.

63. Physics, M. D. o., Pulsed Nuclear Magnetic Resonance: Spin Echoes. **2017**.
64. Zhang, B. O., Xing; Zheng, Jun-chao; Chao, shen; Ming, Lei; Han, Ya-dong; Wang, Jian-long; Qin, Shan-e Electrochemical properties of Li<sub>2</sub>FeP<sub>2</sub>O<sub>7</sub> cathode material synthesized by using different lithium sources. *Electrochimica Acta* **2014**, *133*, 1-7.
65. Lacabanne, D. Solid-state NMR studies of the ABC transporter BmrA in its lipid environment. 2017.
66. Zhang, B.; Ou, X.; Zheng, J.-c.; shen, C.; Ming, L.; Han, Y.-d.; Wang, J.-l.; Qin, S.-e., Electrochemical properties of Li<sub>2</sub>FeP<sub>2</sub>O<sub>7</sub> cathode material synthesized by using different lithium sources. *Electrochimica Acta* **2014**, *133*, 1-7.
67. Ge, Y.; Yan, X.; Liu, J.; Zhang, X.; Wang, J.; He, X.; Wang, R.; Xie, H., An optimized Ni doped LiFePO<sub>4</sub>/C nanocomposite with excellent rate performance. *Electrochimica Acta* **2010**, *55* (20), 5886-5890.
68. Dupin, J.-C.; Gonbeau, D.; Vinatier, P.; Levasseur, A., Systematic XPS studies of metal oxides, hydroxides and peroxides. *Physical Chemistry Chemical Physics* **2000**, *2* (6), 1319-1324.
69. Bard, A. J. L. R. F., Electrochemical Methods: Fundamentals and Applications (2 ed.). **2000**.
70. Dupré, N.; Martin, J.-F.; Guyomard, D.; Yamada, A.; Kanno, R., Characterization of interphases appearing on LiNi<sub>0.5</sub>Mn<sub>0.5</sub>O<sub>2</sub> using <sup>7</sup>Li MAS NMR. *Journal of Power Sources* **2009**, *189* (1), 557-560.
71. Tucker, M.; Doeff, M.; Richardson, T.; Finones, R.; Reimer, J.; Cairns, E., <sup>7</sup>Li and <sup>31</sup>P Magic Angle Spinning Nuclear Magnetic Resonance of LiFePO<sub>4</sub>-type materials. *Electrochemical and Solid State Letters* **2001**, *5*.